Open access • Journal Article • DOI:10.1088/0004-637X/748/2/133

Temporal and spectral evolution in X- and gamma-rays of magnetar 1E 1547.0-5408 since its October 2008 outburst: the discovery of a transient hard pulsed component after its January 2009 outburst — Source link

L. Kuiper, W. Hermsen, P. R. den Hartog, Johnson O. Urama

Institutions: Stanford University, University of Nigeria, Nsukka

Published on: 26 Jan 2012 - arXiv: High Energy Astrophysical Phenomena

Topics: Magnetar and Swift Gamma-Ray Burst Mission

The Astrophysical Journal, 748:133 (21pp), 2012 April 1 doi:10.1088/0004-637X/748/2/133

TEMPORAL AND SPECTRAL EVOLUTION IN X- AND γ-RAYS OF MAGNETAR 1E 1547.0−5408 SINCE ITS 2008 OCTOBER OUTBURST: THE DISCOVERY OF A TRANSIENT HARD PULSED COMPONENT AFTER ITS 2009 JANUARY OUTBURST

L. Kuiper[1], W. Hermsen[1,2], P. R. den Hartog[3], and J. O. Urama[4]
[1] SRON-National Institute for Space Research, Sorbonnelaan 2, 3584 CA, Utrecht, The Netherlands; L.M.Kuiper@sron.nl
[2] Astronomical Institute "Anton Pannekoek," University of Amsterdam, Science Park 904, 1098 XH Amsterdam, The Netherlands
[3] Stanford University HEPL/KIPAC Physics, 382 via Pueblo Mall Stanford, CA 94305, USA
[4] Department of Physics & Astronomy, University of Nigeria, Nsukka, Nigeria
Received 2011 November 3; accepted 2012 January 24; published 2012 March 15

ABSTRACT

The magnetar 1E 1547.0−5408 exhibited outbursts in 2008 October and 2009 January. In this paper, we present in great detail the evolution of the temporal and spectral characteristics of the persistent *total* and *pulsed* emission of 1E 1547.0−5408 between ∼1 and 300 keV starting on 2008 October 3 and ending in 2011 January. We analyzed data collected with the *Rossi X-ray Timing Explorer* (*RXTE*) the *International Gamma-Ray Astrophysics Laboratory* (*INTEGRAL*), and the *Swift* satellite. We report the evolution of the pulse frequency, and the measurement at the time of the onset of the 2009 January outburst of an insignificant jump in frequency, but a major frequency derivative jump $\Delta\dot{\nu}$ of $+(1.30 \pm 0.14) \times 10^{-11}$ Hz s^{-1} ($\Delta\dot{\nu}/\dot{\nu}$ of -0.69 ± 0.07). Before this $\dot{\nu}$ glitch, a single broad pulse is detected, mainly for energies below ∼10 keV. Surprisingly, ∼11 days after the glitch a new transient high-energy (up to ∼150 keV) pulse appears with a Gaussian shape and width 0.23, shifted in phase by ∼0.31 compared to the low-energy pulse, which smoothly fades to undetectable levels in ∼350 days. We report the evolution of the *pulsed*-emission spectra. For energies 2.5–10 keV all *pulsed* spectra are very soft with photon indices Γ between −4.6 and −3.9. For ∼10–150 keV, after the $\dot{\nu}$ glitch, we report hard non-thermal *pulsed* spectra, similar to what has been reported for the persistent pulsed emission of some anomalous X-ray pulsars. This pulsed hard X-ray emission reached maximal luminosity 70 ± 30 days after the glitch epoch, followed by a gradual decrease by more than a factor of 10 over ∼300 days. These characteristics differ from those of the *total* emission. Both, the *total* soft X-ray (1–10 keV) and hard X-ray (10–150 keV) fluxes, were maximal already 2 days after the 2009 January outburst, and decayed by a factor of $\gtrsim$3 over ∼400 days. The *total* spectra can be described with a blackbody (kT values varying in the range 0.57–0.74 keV) plus a single power-law model. The photon index exhibited a hardening (∼−1.4 to ∼−0.9) with time, correlated with a decrease in flux in the 20–300 keV band. We discuss these findings in the framework of the magnetar model.

Key words: pulsars: individual (1E 1547.0−5408, SGR J1550−5418, 1RXS J1708−4009, 4U 0142+61, 1E 1841−045) – X-rays: stars

1. INTRODUCTION

Over the last decade, observational evidence has mounted that anomalous X-ray pulsars (AXPs) and soft gamma-ray repeaters (SGRs) belong to the same class of objects. Most publications discuss these objects in the framework of strongly magnetized neutron stars, dubbed magnetars (Duncan & Thompson 1992; Thompson & Duncan 1995). Alternative interpretations exist including "normal" magnetized neutron stars with fall-back disks (e.g., Chatterjee et al. 2000; Alpar 2001), white dwarfs (e.g., Malheiro et al. 2011), or even quark stars (e.g., Xu 2007; Orsaria et al. 2011). In this paper, we adopt the magnetar interpretation. Magnetars are rotating neutron stars with surface magnetic field strengths of 10^{14}–10^{15} G, well above the critical field strength of 4.413×10^{13} G at which the cyclotron energy of an electron reaches the electron rest mass energy. They have long rotation periods P (in the range 2–12 s) and large period derivatives $\dot{P}$ ($\sim 10^{-11}$ s s^{-1}).

Their soft X-ray (<10 keV) luminosities of $\sim 10^{35}$ erg s^{-1} exceed the available rotational energy losses (see reviews by Woods & Thompson 2006; Kaspi 2007; Mereghetti 2008). In addition to SGR giant flares, SGRs and AXPs exhibit periods of high activity wherein radiative outbursts are accompanied by numerous short bursts of typical durations a few hundred milliseconds. In the context of the magnetar twisted magnetosphere model (Thompson et al. 2002), the energy release is due to magnetic field rearrangement which may be triggered by crustal deformation causing a glitch in their rotational timing behavior.

A distinct feature is the high non-thermal luminosity of the persistent emission of AXPs above 20 keV, first established by Kuiper et al. (2004) with the discovery of pulsed hard X-ray emission up to 150 keV from AXP 1E 1841−045 in supernova remnant (SNR) Kes 73. The X-ray luminosity spectrum exhibits two peaks, one near 1 keV and the other above 100 keV (see, e.g., Kuiper et al. 2006; Götz et al. 2006; den Hartog et al. 2008a, 2008b; Enoto et al. 2010b). The soft X-ray part of the spectrum below 10 keV and the hard X-ray part above 20 keV both exhibit luminosities exceeding the spin-down power by one to three orders of magnitude. The spectra of the first component can be empirically described by a thermal blackbody (BB) plus a soft power-law (Pl; index 2–4) model or two BB models, and more physically with resonant cyclotron scattering models (Thompson et al. 2002; Lyutikov & Gavriil 2006; Fernandez & Thompson 2007; Güver et al. 2007, 2008; Rea et al. 2008; Nobili et al. 2008; Zane et al. 2009, 2011).

On the origin of the hard non-thermal persistent component above ∼10 keV, however, no consensus has been reached. It has been shown (den Hartog et al. 2008a, 2008b) that this component is persistent and within the statistical errors of about 20% stable over years, possibly as long as a decade, in both total and pulsed fluxes and spectral shapes, as well as in pulse

phase/shape. Most recent attempts to explain these findings in the magnetar interpretation are by Beloborodov & Thompson (2007), Beloborodov (2009), Baring & Harding (2007, 2008), and Pavan et al. (2009). The non-thermal component above 10 keV has also been discussed in the context of the fall-back disk model (Trümper et al. 2010a, 2010b). In his latest work, Beloborodov (2009, 2011) discusses how a "starquake" can cause convective motions in the crust which twist the magnetic field anchored to the surface, after which it gradually untwists, dissipating magnetic energy, and producing radiation. A current-carrying bundle of closed field lines ("j-bundle") is created above the magnetic dipole axis. Part of the thermal X-rays emitted by the neutron star are upscattered by the inner relativistic outflow in the quasi-steady j-bundle, producing a beam of hard X-rays.

In this context, it is therefore of great interest to study the evolution of the observational characteristics of a magnetar before and after a glitch followed by a radiative outburst; to study the spectral variations in the persistent steady and pulsed emissions in the soft and hard X-ray bands, as well as variations in pulse profile. So far the decay from a radiative outburst could only be studied in detail for energies below ∼10 keV, e.g., for 1E2259+586 (Woods et al. 2004), SGR 0501+4516 (Rea et al. 2009; Göğüş et al. 2010b), SGR J1833−0832 (Göğüş et al. 2010a; Esposito et al. 2011), SGR 1900+14 (Göğüş et al. 2011), and CXOU J164710.2−455216 (Woods et al. 2011). In this work, we present the first study in which both the temporal and spectral characteristics at both soft and hard X-ray energies before and during a radiative outburst of a magnetar, 1E 1547.0−5408, have been derived.

The X-ray source 1E 1547.0−5408 was discovered by Lamb & Markert (1981) in an *Einstein* HRI observation. Based on its X-ray spectrum and variability, Gelfand & Gaensler (2007) discussed this source as candidate magnetar in a candidate SNR (G327.24−0.13). Subsequently, its period was discovered in the radio band by Camilo et al. (2007), making it the first magnetar of which the pulsation was not discovered at X-ray energies, and the second known radio-emitting magnetar after the transient XTE J1810−197 (Camilo et al. 2006). With the reported period of 2.069 s it appeared to be the fastest spinning magnetar known, with a derived surface magnetic dipole field strength of 2.2×10^{14} G, a characteristic age of 1.4 kyr, and a spin-down luminosity of 1.0×10^{35} erg s^{-1}, assuming a distance of ∼9 kpc (estimated from the dispersion measure). X-ray pulsations were first detected with *XMM-Newton* by Halpern et al. (2008) in a period of enhanced activity in 2007. These authors concluded that the source was recovering from an X-ray outburst between 2006 and 2007.

On 2008 October 3 (MJD 54742) 1E 1547.0−5408, later dubbed SGR J1550−5418, started a period of strong bursting activity detected by *Swift* (Krimm et al. 2008a, 2008b; Israel et al. 2010), and by the Gamma-ray Burst Monitor (GBM) on the *Fermi Gamma-ray Space Telescope* (von Kienlin & Briggs 2008; Kaneko et al. 2010). The bursting activity was accompanied by a radiative outburst which was also detected with the *Rossi X-ray Timing Explorer* (*RXTE*) and *Chandra* (Ng et al. 2011). Israel et al. (2010) used *Swift* and Ng et al. (2011) used *RXTE* and *Chandra* data to study the evolution of the pulse profile shape and the phase-averaged spectrum for energies below 10 keV during the outbursting activity.

The *Swift* Burst Alert Telescope (BAT) reported renewed extreme bursting activity starting on 2009 January 22 (MJD 54853; Gronwall et al. 2009), also detected by *INTEGRAL* (Savchenko et al. 2009; Mereghetti et al. 2009a), the *Fermi*/GBM (Connaughton & Briggs 2009), Konus-*Wind* (Golenetskii et al. 2009), *RHESSI* (Bellm et al. 2009), and the Wide-band All-sky Monitor on board *Suzaku* (Terada et al. 2009). Follow-up observations with *Swift* and *XMM-Newton* revealed dust scattering X-ray rings centered on 1E 1547.0−5408, from which Tiengo et al. (2010) deduced a source distance of ∼3.9 kpc. Based on a 100 ks public target-of-opportunity (ToO) *INTEGRAL* observation, Baldovin et al. (2009) reported the discovery of a hard power-law tail in the spectrum. Exploiting also part of our 600 ks *INTEGRAL* open-time (PI: den Hartog) ToO observations, a power-law index of ∼1.5 was found for energies from 20 up to 150 keV from two to seven days after the 2009 January outburst (den Hartog et al. 2009). This was confirmed in *Suzaku* observations taken seven days after the outburst (Enoto et al. 2010a). Furthermore, Kuiper et al. (2009) announced the detection with *INTEGRAL* of pulsed emission for energies up to 150 keV.

Enoto et al. (2010a) presented the *Suzaku* results on AXP 1E 1547.0−5408 for their observations seven days after the onset of the bursting activity in 2009. Pulsations were detected for energies up to 70 keV, and the total, time-averaged 0.7–114 keV spectrum was discussed. Ng et al. (2011) compared the 2008 and 2009 outbursts, analyzing *RXTE* and *Chandra* observations taken during ∼20 days after the onset of the bursting activities in 2008 and 2009, comparing pulse profiles, pulsed-emission spectra below 10 keV, and spin evolution. Furthermore, Bernardini et al. (2011) monitored the 2009 outburst with *Chandra*, *XMM-Newton*, and *INTEGRAL* over a period of two weeks after the onset, as well as with *Swift* over a 1.5 year interval. Finally, Scholz & Kaspi (2011) focused on the 2009 outburst using *Swift* X-Ray Telescope (XRT) observations for energies below 10 keV addressing the persistent radiative evolution and a statistical study of the burst properties.

In this work we exploited the extensive database of observations of 1E 1547.0−5408 with *RXTE*, *INTEGRAL*, and *Swift*, covering 27 months from the onset of the bursting activities in 2008 October until 2011 January. We studied in detail the variable (total and pulsed) emission, but did not address the burst properties (see, e.g., Savchenko et al. 2010; Mereghetti et al. 2009b; Kaneko et al. 2010). The evolution of the timing parameters, pulse profiles, fluxes, and spectra have been derived over the broad energy range ∼1–300 keV. Particularly interesting is the discovery of a transient non-thermal hard X-ray component, which appeared shortly after the onset of 2009 January 22 outburst, triggered by a $\dot{\nu}$ timing glitch, as a distinct new pulse in the pulse profile. Finally, our findings are summarized in Section 6 and are compared with model predictions within the magnetar framework.

2. INSTRUMENTS AND OBSERVATIONS

2.1. Rossi X-Ray Timing Explorer

In this study, extensive use is made of data from monitoring observations of AXPs with the two non-imaging X-ray instruments aboard *RXTE*, the Proportional Counter Array (PCA; 2–60 keV) and the High-Energy X-Ray Timing Experiment (HEXTE; 15–250 keV).

2.1.1. RXTE/PCA

The PCA (Jahoda et al. 1996) consists of five collimated Xenon Proportional Counter Units (PCUs) with a total effective

Table 1
List of *RXTE* Observations of 1E 1547.0−5408 Used in This Study

Observation Identifier	Begin/End Date (yyyy-mm-dd)	Exp.[a] (ks)
20060	1997-05-15/1997-05-15	0.376[b]
93017	2008-10-03/2009-01-24	162.484
94017	2009-01-25/2009-06-22	174.676
94427	2009-06-30/2009-12-26	104.677
95312	2010-01-04/2010-12-25	236.952
93017–95312	2008-10-03/2010-12-25	678.789

Notes.
[a] PCU-2 exposure after screening.
[b] Scanning observation.

area of ∼6500 cm^2 over a ∼1° (FWHM) field of view. Each PCU has a front propane anti-coincidence layer and three Xenon layers which provide the basic scientific data, and is sensitive to photons with energies in the range 2–60 keV. The energy resolution is about 18% at 6 keV. All PCA data used in this study have been collected from observations in `GoodXenon` mode, allowing high-time resolution (0.9 μs) analyses in 256 spectral bins. Since the launch of *RXTE* on 1995 December 30 the PCA has experienced high voltage breakdowns for all constituting PCUs at irregular times. To avoid further breakdowns, during its already 14.5 year mission not all PCUs are simultaneously operating. The most stable PCU is PCU-2, which is on for almost all of the time. On average, one (50%) or two (40%) PCUs is/are operational during a typical observation.

2.1.2. RXTE-HEXTE

The HEXTE instrument (Rothschild et al. 1998) consists of two independent detector clusters A and B, each containing four Na(Tl)/CsI(Na) scintillation detectors. The HEXTE detectors are mechanically collimated to a ∼1° (FWHM) field of view and cover the 15–250 keV energy range with an energy resolution of ∼15% at 60 keV. The collecting area is 1400 cm^2, taking into account the loss of the spectral capabilities of one of the detectors. The maximum time resolution of the tagged events is 7.6 μs. In its default operation mode, the field of view of each cluster is switched on and off source to provide instantaneous background measurements. However, HEXTE also suffers from aging, and since 2006 July 13 HEXTE cluster-A operates in staring mode at an on-source position, while on 2010 March 29 cluster-B was commanded to stare at an off-source position.

Due to the co-alignment of HEXTE and the PCA, they simultaneously observe celestial targets. Table 1 lists the *RXTE* observations used in this study. The third column shows the screened exposure of PCU-2 (see Section 3). A typical observation consists of several sub-observations spaced more or less uniformly (four to nine days apart) between the start and end dates of the observation cycle. However, for a ∼2–3 week time period directly after the two outbursts intensive timing has been performed.

2.2. INTEGRAL

The *INTEGRAL* spacecraft (Winkler et al. 2003), launched on 2002 October 17, carries two main γ-ray instruments: a high-angular-resolution imager, IBIS (Ubertini et al. 2003), and a high-energy-resolution spectrometer, SPI (Vedrenne et al. 2003). The payload is further supported by two monitor instruments providing complementary observations in the X-ray and optical energy bands, the Joint European Monitor for X-rays (JEM-X; Lund et al. 2003) and the Optical Monitoring Camera (OMC; 500–600 nm, Johnson *V*-filter). All the high-energy instruments make use of coded aperture masks enabling image reconstruction in the hard X-ray/soft γ-ray band.

Table 2
List of *INTEGRAL* Observations of 1E 1547.0−5408 Used in This Work, Sorted on *INTEGRAL* Orbital Revolutions

Revs.	Begin/End Date (yyyy-mm-dd)	Begin/End (MJD)	Exp.[a] (ks)	ID
731	2008-10-08/2008-10-10	54747.9/54749.2	98.4	1
767	2009-01-24/2009-01-25	54855.6/54856.9	92.6	2
768–772	2009-01-28/2009-02-08	54859.6/54870.7	575.6	3
782–791	2009-03-09/2009-04-08	54899.6/54929.0	191.9	4
840–850	2009-08-30/2009-10-01	55073.6/55105.5	407.8	5
899–910	2010-02-23/2010-03-29	55250.3/55284.3	524.0	6
911–912	2010-03-30/2010-04-03	55285.9/55289.0	193.7	7

Notes. In the last two columns, the exposures and time segment identifiers are given.
[a] Effective on-axis exposure.

In our study, guided by sensitivity considerations, we only used data recorded by the *INTEGRAL* Soft Gamma-Ray Imager ISGRI (Lebrun et al. 2003), the upper detector system of IBIS, sensitive to photons with energies in the range ∼20 keV–1 MeV, and JEM-X operating in the 3–35 keV X-ray band.

With an angular resolution of about 12′ and a source location accuracy of better than 1′ (for a $>10\sigma$ source) ISGRI is able to locate and separate high-energy sources in crowded fields within its 19° × 19° field of view (50% partially coded) with an unprecedented sensitivity (∼960 cm^2 at 50 keV). Its energy resolution of about 7% at 100 keV is amply sufficient to determine the (continuum) spectral properties of hard X-ray sources in the ∼20–300 keV energy band.

The timing accuracy of the ISGRI time stamps recorded on board is about 61 μs. The time alignment between *INTEGRAL* and *RXTE* is better than ∼50 μs, verified using data from simultaneous *RXTE* and *INTEGRAL* observations of the accretion-powered millisecond pulsars IGR J00291+5934 (Falanga et al. 2005) and IGR J17511−3057 (Falanga et al. 2011).

JEM-X consists of two identical telescopes each having a field of view of 7.°5 (diameter) at half response and able to pinpoint a 15σ source with a 90% location accuracy of about 1′. Its energy resolution and timing accuracy (3σ) are 1.3 keV at 10 keV and 122.1 μs, respectively.

In its default operation mode *INTEGRAL* observes the sky in a dither pattern with 2° steps, which could be rectangular, e.g., a 5 × 5 dither pattern with 25 grid points, or hexagonal with 7 grid points (target in the middle). Typical integration times for each grid point (pointing/sub-observation) are in the range 1800–3600 s. This strategy drives the structure of the *INTEGRAL* data archive, which is organized in so-called science windows (Scw) per *INTEGRAL* orbital revolution (lasting for about three days) containing the data from all instruments for a given pointing. Most of the *INTEGRAL* data reduction in this study was performed with the Offline Scientific Analysis (OSA) version 7.0 distributed by the *INTEGRAL* Science Data Centre (ISDC; see, e.g., Courvoisier et al. 2003).

Table 2 lists the *INTEGRAL* orbital revolution (Rev.) identifiers with corresponding start/end dates of the observations used in the imaging/spectral analyses and/or timing analyses of 1E 1547.0−5408. Revs. 731 (2008 October; ToO), 767 (2009 January; public ToO), 768–772 (2009 January–February;

ToO), and 911–912 had 1E 1547.0−5408 as on-axis prime target, while during Revs. 782–791, 840–845/850, and 899–910 (all part of an *INTEGRAL* key program to observe deeply the $l = \pm 25$ Galactic plane region) 1E 1547.0−5408 was in the field of view at moderate off-axis angles.

2.3. Swift

The *Swift* satellite (Gehrels et al. 2004) was launched on 2004 November 20 and regular observations began on 2005 April 5. The main goal of the mission is the study of gamma-ray bursts and their afterglows. *Swift* carries three co-aligned instruments: the wide-field coded aperture mask BAT (15–150 keV), the narrow field ($23\farcm6 \times 23\farcm6$) grazing incidence Wolter 1 XRT (0.2–10 keV), and the Ultraviolet/Optical Telescope (UVOT).

During periods of non-burst operations, observations of other high-energy sources are scheduled. In this work, we used data of 1E 1547.0−5408 gathered by the XRT (Burrows et al. 2005).

Regular monitoring of 1E 1547.0−5408 commenced on 2007 June 22 following the detection of radio pulsations on 2007 June 8 (Camilo et al. 2007). The XRT has several operation modes of which we used only the Windowed Timing (WT) and Photon-counting (PC) modes. In the PC mode full imaging (600×600 pixels; pixel scale $2\farcs36$ pixel^{-1}) and spectroscopic resolution are retained, but its time resolution is only 2.5073 s, insufficient to detect the pulsations of 1E 1547.0−5408. In the WT mode 10 rows are compressed in one, and only the central 200 columns are read out. Therefore, only a $\sim 8'$ central strip of the field of view is covered. The time resolution in the WT mode, however, is 1.7675 ms amply sufficient for pulse timing studies of 1E 1547.0−5408.

Intensive monitoring data are available for two-to-three week time periods directly after the onsets of the 2008 October and 2009 January outbursts. We used the XRT WT data gathered between 2008 October 3 and 24 (*Swift* observation IDs 00330353000–00330353016; MJD 54742–54763) for a combined *RXTE*/PCA/*Swift*/XRT timing study of the pulsed signal at soft X-rays.

From the onset of the 2009 January outburst on 2009 January 22 until 2009 February 7, 1E 1547.0−5408 was observed daily by the XRT both in the WT and PC modes. This period of dense sampling was followed by monitoring observations taken at a rate of roughly one to four times per month in either WT or PC mode, and this strategy continues up to now. XRT WT data gathered between 2009 January 22 and 2009 February 22 (MJD 54853–54884) have been used in the construction of timing models in combination with *RXTE*/PCA data.

Data taken in the PC mode on 2009 January 25 and 29 and February 4 (*Swift* observation IDs 00341114000, 00030956034, and 00030956039, respectively), covering the time window for which we have deep *INTEGRAL* observations (see Table 2; 2009 January 24–February 8, i.e., MJD 54855.6–54870.7), have been employed in spectral analyses of the *total* soft X-ray emission of 1E 1547.0−5408. Furthermore, to study the evolution of the total soft X-ray spectrum we analyzed *Swift*/XRT observations 00030956048 (2009 July 8), 00030956051 (2009 August 19), 00090404003 (2010 April 12), 00090404019 (2010 September 28), and 00090404027 (2011 February 25).

Finally, XRT observations in the WT mode performed between 2009 January 4 and 13 and after 2009 February 22 have been used for verification purposes of timing models based on merely *RXTE* (monitoring) observations. The latter are sampled too sparsely given the high level of timing noise (Camilo et al. 2008) present in this source.

3. TIMING, TOTAL FLUX, AND PULSED-FLUX EVOLUTIONS BELOW ∼10 keV

We exploited the regular monitoring observations with the PCA on *RXTE* over more than two years (see Table 1) that provided the required high-statistics data. Because the number of active PCUs at any time was changing, we treated the five PCUs constituting the PCA separately. Good time intervals (GTIs) have been determined for each PCU by including only time periods when the PCU in question is on, and during which the pointing direction is within $0\fdg05$ from the target, the elevation angle above Earth's horizon is greater than 5°, a time delay of 30 minutes since the peak of a South-Atlantic-Anomaly passage holds, and a low background level due to contaminating electrons, as measured by PCU-2, is observed. Furthermore, periods during which a detector breakdown (see Section 2.1.1) has occurred are excluded for further analysis. Finally, because we are only interested in the persistent non-burst emission properties, we rejected short-duration ($\leqslant 1$ s) bursts. The latter filtering is especially important just after the onset of the 2008 October and 2009 January outbursts when copious numbers of bursts are detected. The resulting GTIs have subsequently been applied in the screening process to the data streams from each of the PCUs (e.g., see Table 1 for the resulting screened exposure of PCU-2 per observation cycle).

The TT (Terrestrial Time) arrival times of the selected events (for each sub-observation and PCU unit) were converted to arrival times at the solar system barycenter (in Barycentric Dynamical Time (TDB) timescale) using (1) the JPL DE200 solar system ephemeris, (2) the instantaneous spacecraft position, and (3) the subarcsecond celestial position of 1E 1547.0−5408. The position used is $(\alpha, \delta) = (15^{\rm h}50^{\rm m}54\fs11, -54°18'23\farcs7)$ for epoch J2000 (Camilo et al. 2007), which corresponds to $(l, b) = (327.23705, -0.13162)$ in Galactic coordinates.

3.1. Total Flux Evolution at X-Rays below ∼10 keV

From the screened event data sets and the breakdown/burst-corrected exposure times, we could derive the total count rate from a circular field with a radius of ∼1° (PCA field of view up to zero collimator response) on 1E 1547.0−5408. We determined this for the 4–27 pulse-height analyzer (PHA) channel range (∼2–10 keV) including all Xenon detector layers. The count rate includes the instrumental and celestial (Galactic diffuse) background, emission from 1E 1547.0−5408 and its pulsar wind nebula (PWN)/SNR (Vink & Bamba 2009) and other discrete point sources. We found in the archive two *RXTE* scanning observations, both performed on 1997 May 15, with 1E 1547.0−5408 in the field of view for 40 s (screened) at $28\farcm1$ offset angle and 336 s (screened) at $17\farcm3$ offset angle. We used the count rate from the combination of these two scanning observations as reference because the source at that time was very likely in quiescence.

The total flux evolution, from 2008 October 3 up to 2010 December 25, of 1E 1547.0−5408 above the reference level of 9.70 ± 0.16 c s^{-1} as measured by PCU-2 in the 4–27 PHA range (all detector layers) is shown in the top panel of Figure 1.

We cropped this figure in the vertical direction in order to better visualize the late-time evolution (the count rate of 44.19(8) measured directly after the 2009 January 22 outburst at MJD 54853.911 is off scale). The onsets of the 2008 October 3 and 2009 January 22 outbursts are indicated in this figure. There is a monitoring gap of about a month which occurred in 2009 September/October due to *RXTE* spacecraft anomalies.

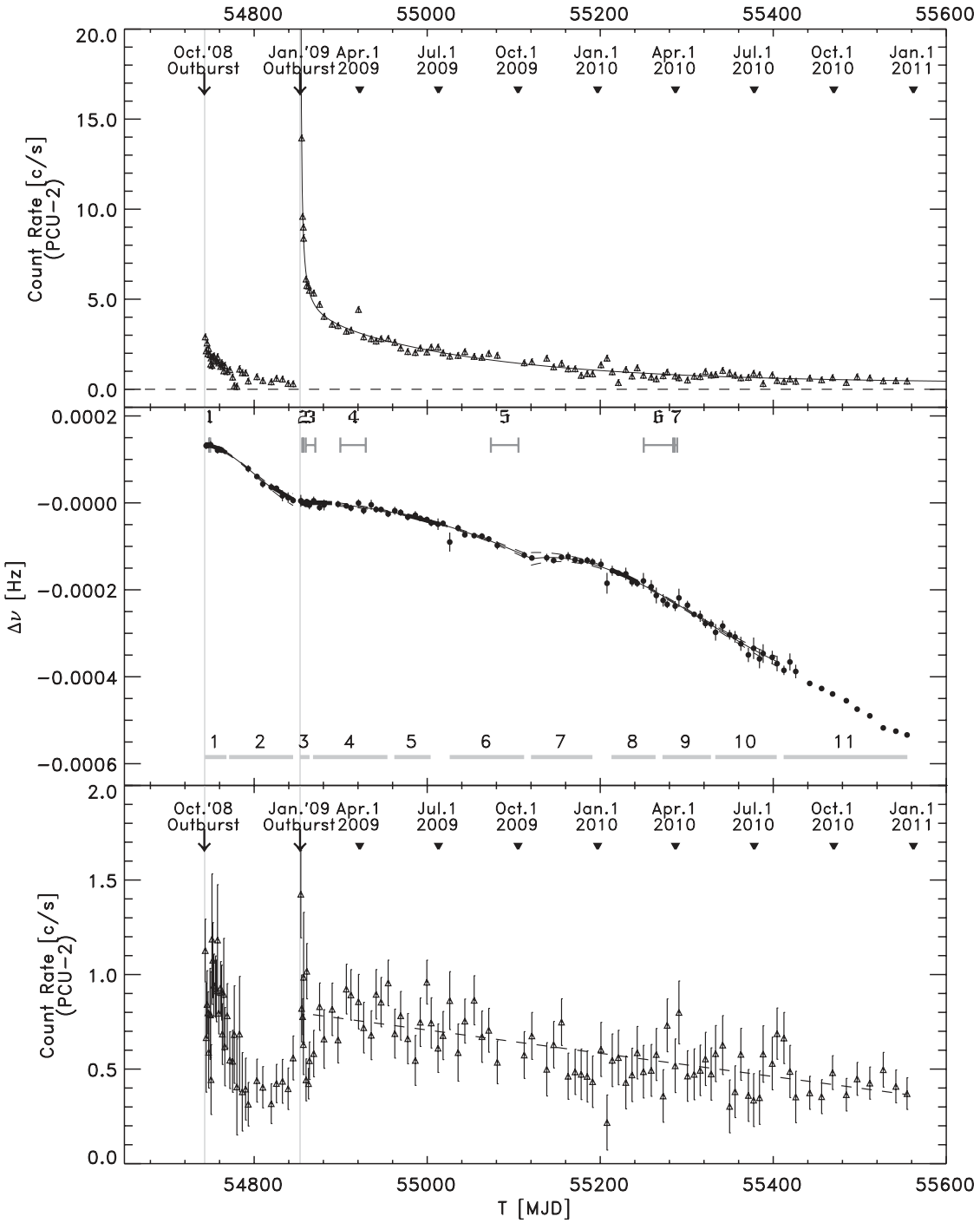

Figure 1. Evolution of the total flux (top panel) and pulsed flux (bottom panel) of 1E 1547.0−5408 from 2008 October 3 until 2010 December 25 as measured by the PCA/PCU-2, summing the signals from all three detection layers for the pulse-height-channel range 4–27 (∼2–10 keV). We have subtracted the 1997 pre-outburst reference level (see Section 3.1) for the total rate (top panel; dashed line) and superposed the best-fit decay model as a solid line (top panel). The middle panel shows the frequency measurements (data points), three incoherent fit segments (solid plus dashed lines (=1σ uncertainty)), and five bold segments representing reliable coherent timing solutions. Time intervals for which detailed PCA pulse morphology and spectral studies were performed are labeled at the bottom of the middle panel (11 segments). At the top of the middle panel, seven intervals are shown for which *INTEGRAL* observations are available (see Table 2). The dashed line in the bottom panel represents the best fit of a linear decay model for the period MJD 54868–55555.

It is clear that since 2008 October 3 the total flux decayed to almost its reference level just before the 2009 January 22 outburst. The flux decay of the much more intense second outburst, however, has still not reached its reference level ∼2 year after the onset. We studied the decay of the total flux since the 2009 January 22 outburst in more detail by fitting the data, excluding the time intervals in which the mini-outbursts occurred (see Section 3.1.1), with a model composed of a constant, an exponential, and a power-law-like decay component:

$$R_{\rm tot}(t) = a + b \cdot \left(1 + \frac{t - t_0}{\tau_0}\right)^{\alpha} + c \cdot \exp\left(-\frac{t - t_0}{\tau_1}\right). \quad (1)$$

We fixed t_0 at MJD = 54853.035, used only times with $t \geqslant 54854$ (MJD), and fitted the six free parameters to obtain the

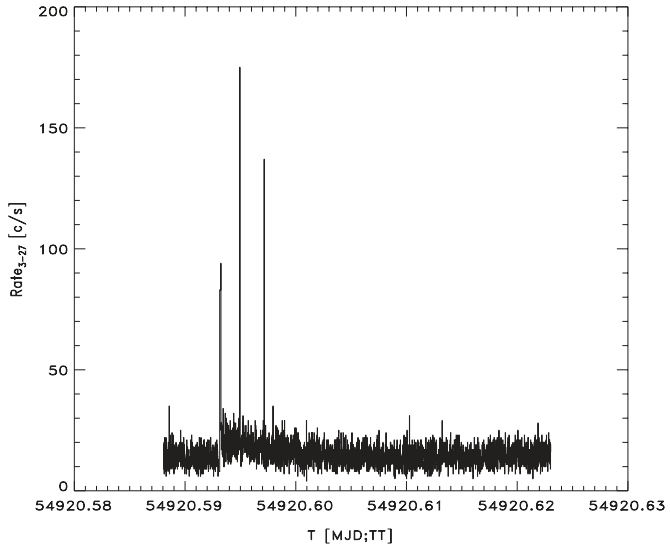

Figure 2. Count rate of 1E 1547.0−5408 in the 3–27 PHA range (all detector layers combined) as observed by the PCU-2 during observation 94017-09-09-00 on 2009 March 30 (MJD 54920). The time bin width is 1 s. The time is expressed in MJD for the TT time system. Note the enhanced emission level of ∼450 s duration with superposed three short bursts.

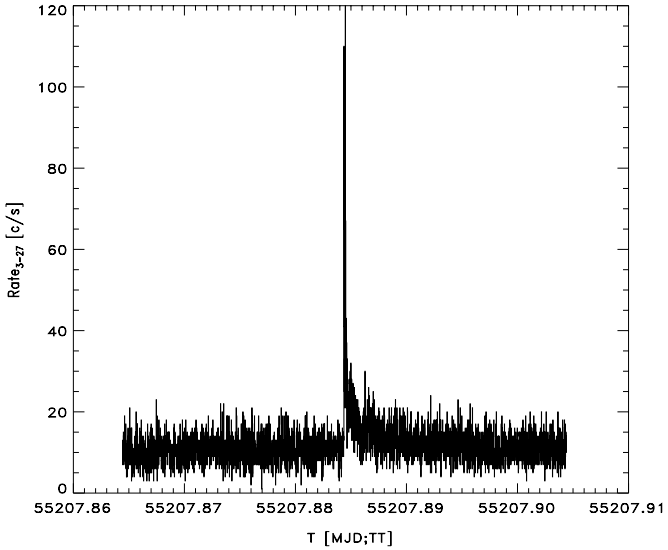

Figure 3. Count rate of 1E 1547.0−5408 for the observation 95312-01-02-00 on 2010 January 11 (MJD 55207) as in Figure 2. Note the enhanced emission level of ∼130 s duration with superposed two bursts separated at 11 s (not resolved at the displayed scale).

best description of the observed decay. We found the following optimized parameters: $a = 0.33 \pm 0.05$ c s^{-1}, $b = 152.5 \pm 4.4$ c s^{-1}, $c = 3.5 \pm 0.1$ c s^{-1}, $\tau_0 = 0.129 \pm 0.004$ days, $\tau_1 = 207 \pm 11$ days, and finally $\alpha = -1.01 \pm 0.01$ (errors are 1σ), for a fit with a reasonable quality of $\chi^2_v = 138.58/82 = 1.69$. This model is superposed in the top panel of Figure 1 as a solid line, and follows the measurements globally pretty well. The slowly decaying exponential component has a timescale of typically ∼200 days, whereas the rapidly decaying power-law component contributes only significantly to the total flux for the first ∼50 days since the 2009 January 22 outburst, over which its fractional contribution to the total rate is more than 10%. The power-law component dominates only during a time period of ∼5 days directly after the outburst, then the combination of constant plus exponential component takes over.

3.1.1. Mini-outbursts

A detailed look at the decaying tail of the 2009 January 22 outburst shows a large deviation from the global decay trend near MJD 54920 (2009 March 30). Initially, we believed that we were dealing with a processing error/anomaly, but a deeper investigation revealed a period of enhanced emission of about 450 s with superposed at least three short-duration bursts (see Figure 2). This behavior was seen in both PCU-1 and PCU-2, which were both operational during the observation in question, thus excluding an instrumental (non-celestial) cause of the observed phenomenon. The period of enhanced emission was preceded by a short-duration burst.

We searched for more mini-outbursts and found one on 2010 January 11 (MJD 55207.8845 TT, see Figure 3). Enhanced emission is seen for a period of about 130 s with superposed two bursts with a separation of ∼11 s between the burst maxima.

An interesting feature of this enhanced emission period is that the burst trail is highly pulsed. We found a pulsed signal strength of $\sim 13\sigma$ (see Figure 4) for the burst-cleaned emission confined in a time window of only 52 s starting at the onset of the first burst for the 4–50 PHA range (∼2–20 keV) using all detector layers of PCU-2, the only detector operational during the observation. This proves that the enhanced emission is originating from

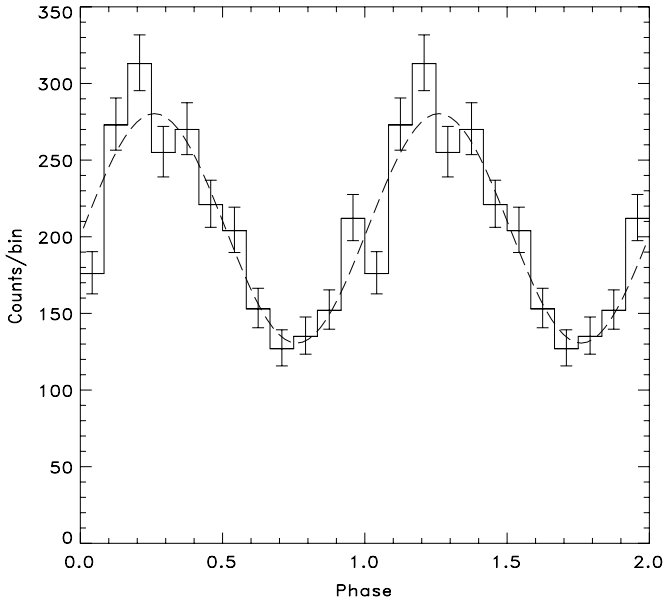

Figure 4. Twelve bin pulse profile of 1E 1547.0−5408 for events with PHA values in the range 4–50 (∼2–20 keV) from any PCU-2 detector layer gathered during a 52 s time period starting at the onset of first burst of the 2010 January 11 mini-outburst. Two cycles are shown for clarity. A sine fit (dashed line) is superposed to guide the eye and to demonstrate that the pulsed emission is highly symmetric. A 13σ signal is detected during this very short time window, indicating the presence of strong pulsating tail emission.

1E 1547.0−5408. Next, we revisited the enhanced emission period observed earlier by the PCA on MJD 54920, but in this case we did *not* find any evidence for highly increased pulsed emission.

Similar behavior has been detected by Kaneko et al. (2010) using *Fermi*/GBM data during a period of enhanced persistent emission of ∼150 s duration starting only 70 s after the first GBM trigger at the onset of the 2009 January 22 outburst.[5] Also, Mereghetti et al. (2009b) reported on pulsating tails

[5] Note that *Fermi*/GBM (all-sky monitor) detected the onset of the 2009 January 22 outburst about 39 minutes earlier than *Swift*/BAT (Gronwall et al. 2009, only one-sixth of the sky is visible by the BAT at any instant).

Table 3
Incoherent Timing Models for 1E 1547.0−5408 as Derived from *RXTE*/PCA Monitoring Data

Entry No.	Start (MJD)	End (MJD)	t_0, Epoch (MJD,TDB)	ν (Hz)	$\dot{\nu}$ ($\times 10^{-12}$ Hz s^{-1})	$\ddot{\nu}$ ($\times 10^{-18}$ Hz s^{-2})	$\dddot{\nu}$ ($\times 10^{-25}$ Hz s^{-3})
1	54743	54845	54780.0	0.482728(2)	−22.3(11)	−2.5(3)	15(4)
2	54896	55121	54995.0	0.482496(2)	−11.0(3)	−0.44(8)	0
3	55120	55404	55270.0	0.482201(2)	−18.1(5)	−0.50(9)	1.2(3)

Table 4
Phase-coherent Ephemerides for 1E 1547.0−5408 as Derived from *RXTE*/PCA and *Swift*/XRT Data

Entry No.	Start (MJD)	End (MJD)	t_0, Epoch (MJD,TDB)	ν (Hz)	$\dot{\nu}$ ($\times 10^{-12}$ Hz s^{-1})	$\ddot{\nu}$ ($\times 10^{-18}$ Hz s^{-2})	Φ_0[a]	Validity Range (days)
1	54743	54779	54743.0	0.48277818(3)	−6.48(5)	−6.46(4)	0.4613	37
2	54819	54845	54819.0	0.48264979(4)	−18.67(4)	0.0 (fixed)	0.7382	27
3	54855	54884	54856.0	0.48259525(1)	−5.12(2)	0.0 (fixed)	0.0710	30
4	54855	54890	54856.0	0.48259518(3)	−4.91(5)	−0.23(4)	0.0711	36
5	54977	55012	54977.0	0.48251286(6)	−11.05(9)	−0.18(7)	0.5144	36
6	55213	55243	55229.0	0.48226226(3)	−15.91(2)	−1.07(12)	0.1590	31

Note. [a] Φ_0 is the phase offset to be applied to obtain consistent phase alignment (see Equation (4) in Section 3.4).

lasting several seconds from two bright bursts occurring on 2009 January 22 detected above 80 keV by SPI-ACS on board the *INTEGRAL* satellite.

It is worth mentioning that given the sparse *RXTE* sampling (about 5 ks of observation time per week, i.e., 0.8% of the time, is devoted to observe 1E 1547.0−5408) we very likely miss a lot of such events, i.e., periods of enhanced persistent emission possibly preceded by a burst event. If such events are accompanied by (micro) glitches, the (very) noisy timing behavior (see also Section 3.2.2), inhibiting the construction of phase-coherent timing models over time stretches longer than about 30 days, can easily be explained.

3.2. Evolution of the Pulse Frequency: Incoherent Measurements

In each *RXTE* sub-observation of 1E 1547.0−5408 a coherent pulsed signal at a rate of ∼0.482 Hz (see Camilo et al. 2007) could be detected in the barycentered time series. We used a Z_1^2-test (Buccheri et al. 1983) search in a small, typically five independent Fourier steps[6] wide, window around the predicted pulse frequency. The restricted search yielded for each sub-observation a best estimate of the rotation rate at the gravity point of the sub-observation. Because the Z_1^2-test is distributed as a χ^2 for 2×1 degrees of freedom, a 1σ error estimate on this optimum value can easily be derived by determining the intersection points of the measured Z_1^2-test distribution near the optimum with the value of $Z^2_{1,\max} - 2.296$.

The pulse frequency measurements for 1E 1547.0−5408 from 2008 October 3 until 2010 December 25 are shown as bold data points along with their 1σ errors in the middle panel of Figure 1. The measurements are relative to a coherent model (see later in Section 3.2.2), which could be constructed for the time period MJD 54855–54884 (entry 3 in Table 4), just after the onset of the 2009 January 22 outburst, using both *RXTE*/PCA and *Swift*/XRT data.

3.2.1. Incoherent Models

It is clear from the behavior of the pulse frequency displayed in Figure 1 (middle panel) that we can identify three time periods in which the spin behavior can be described with only a limited number of parameters. Apparent discontinuities in the timing behavior (glitches) are present near MJD 54853, i.e., the onset of the 2009 January 22 outburst, and near MJD 55121 (2009 October 17).

The frequency behavior in each of the three time intervals was determined by fitting the measured pulse frequencies and their 1σ uncertainties by a simple timing model (Taylor series) with either three or four timing parameters (ν, $\dot{\nu}$, $\ddot{\nu}$, [$\dddot{\nu}$]):

$$\nu_{\rm inc}(t) = \nu + \dot{\nu} \cdot (t - t_0) + \frac{1}{2}\ddot{\nu} \cdot (t - t_0)^2 + \frac{1}{6}\dddot{\nu} \cdot (t - t_0)^3. \quad (2)$$

The three incoherent timing solutions $\nu_{\rm inc}(t)$ are listed in Table 3 and shown in Figure 1 (middle panel) as solid lines together with the 1σ uncertainty band (dashed lines), all relative to the coherent timing model 3 (see Table 4).

3.2.2. Coherent Models: Phase-connected Ephemerides

Very accurate timing models (ephemerides) taking into account every rotation of the neutron star can be obtained by employing phase-coherent timing techniques. This requires a set of pulse arrival times (time of arrival, ToA) which results from a correlation analysis of an instantaneous profile with a template correlation profile. For the phase-coherent timing techniques used in this work, we refer to Section 4.1 of Kuiper & Hermsen (2009). In this study the correlation template is based on *RXTE*/PCA events with measured energies $\lesssim$4.2 keV, corresponding to the 4–10 PHA range, because in this range the morphology of the pulse profile is least (almost not) affected by transient morphology changes (see Section 4), which are prominently present in other bands at higher energies $\gtrsim$4.2 keV. It also facilitates the inclusion of ToAs based on *Swift*/XRT observations because then the PCA and XRT effective energy bands are fully overlapping. The PCA correlation template (PHA 4–10; $\lesssim$ 4.2 keV) is shown in Figure 5 adopting 15 bins, and is based on *RXTE* observations performed a couple of days after the 2009 January 22 outburst.

Reliable phase-coherent timing models are given in Table 4. During a 37 day period after the onset of the 2008 October outburst, 1E 1547.0−5408 was intensively monitored by both *RXTE* and *Swift* (from MJD 54742–54764 only). For this period,

[6] A Fourier step is defined by $\Delta\nu_{\rm IFS} = 1/\tau$, in which τ represents the time span of the data period.

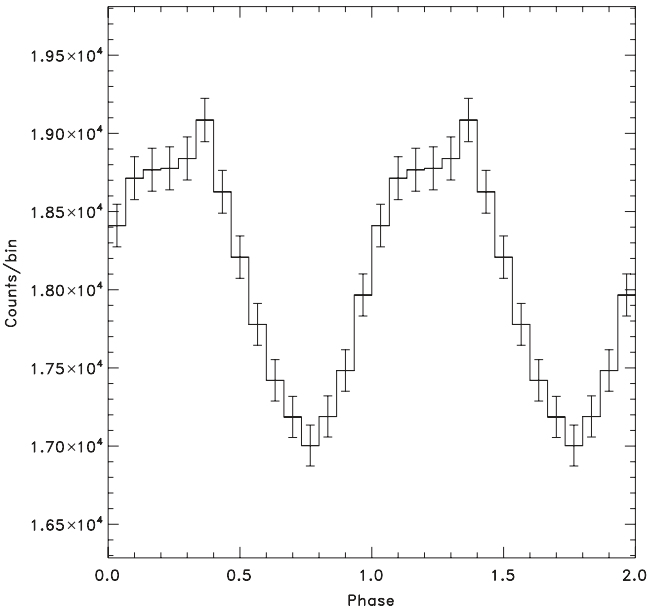

Figure 5. *RXTE*/PCA pulse profile (15 bins) for the PHA range 4–10 (measured energies $\lesssim$ 4.2 keV) used as template in the time-of-arrival (ToA) correlation analysis.

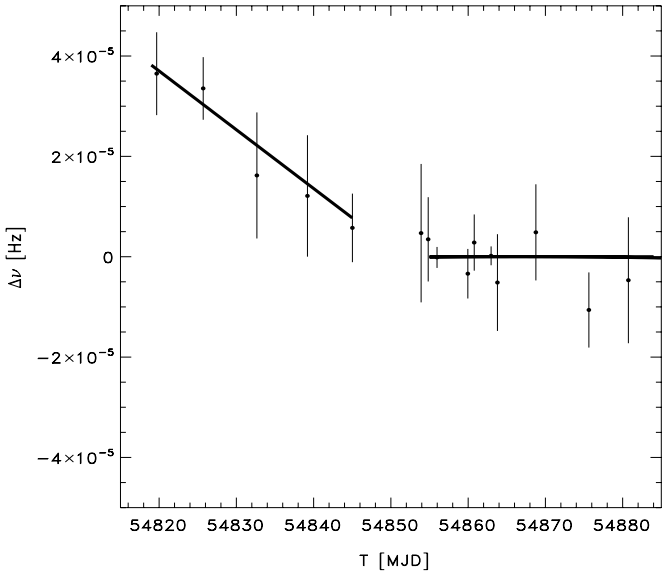

Figure 6. Zoom-in of the rotation frequency behavior around the 2009 January outburst. Frequency measurements are given by the data points, while the solid lines refer to coherent timing models 2 and 3 of Table 4. All frequency values are relative to predictions by model 3. An apparent glitch occurred somewhere between MJD 54845.02 and 54853.91, very likely simultaneously with the onset of the 2009 January outburst at MJD 54853.035 (TDB).

entry 1 of Table 4 specifies the model parameters based on the combined PCA–XRT ToAs set. These are consistent with those published by Ng et al. (2011) and Israel et al. (2010). Note the large negative value for $\ddot{\nu}$ indicating a rapidly increasing spin-down rate.

Entries 3 and 4 of Table 4 show the timing parameters for a period of intensive *Swift* and *RXTE* monitoring (just) after the second outburst in 2009 January, and are valid for a 30 day (two parameters) and 36 day (three parameters) time period, respectively. The timing models are consistent with those reported in Ng et al. (2011) and Bernardini et al. (2011). Comparing these models with the one (entry 2) valid for the period just before the 2009 January outburst, i.e., MJD 54819–54845,[7] indicates that a strong glitch, mainly in $\dot{\nu}$, occurred at a time consistent with the onset of the 2009 January outburst. More details on this apparent glitch are shown later in Section 3.3.1. Finally, the validity of coherent timing models 5 and 6 of Table 4, based on PCA data only, have been verified using independent *Swift*/XRT data taken in the WT mode. Folding these *Swift* data yielded consistent pulse alignment.

Also, for other time intervals with interval lengths of typically 30–35 days we could generate phase-coherent models from PCA data, mostly using two-dimensional (ν, $\dot{\nu}$) optimization schemes applied for a 2σ range around predicted (ν, $\dot{\nu}$) values estimated from an incoherent timing model (see Table 3). However, often due to the lack of independent contemporaneous data from other X-ray instruments, e.g., *Swift*/XRT[8] and given the sparse sampling of the *RXTE* observations, we cannot securely identify the found "best" model as the true underlying rotation model. These models, not listed in Table 4, are still useful for combining *RXTE* observations in spectral studies covering several sub-time intervals.

[7] Two *Swift*/XRT observations in the WT mode have been performed on 2009 January 4 and 13. The pulse profile resulting from the combination of these XRT observations adopting the timing model (entry 2 of Table 4) based on PCA data only shows the expected alignment.

[8] Most of the time *Swift*/XRT operated in the PC mode, inadequate for timing studies of 1E 1547.0−5408.

Finally, for this source phase coherence is typically lost after a ∼30–35 day time period due to the sparse sampling of both *RXTE* and *Swift* observations and the high level of timing noise (see, e.g., Camilo et al. 2008).

3.3. Glitches

3.3.1. The Characteristics of the Glitch Associated with the 2009 January 22 Outburst

In order to study the 2009 January glitch in detail we adopted standard glitch fitting techniques as employed, e.g., in the pulsar timing software package TEMPO2 version 1.9.[9] We use the following, commonly used, expression for the evolution of the frequency crossing a glitch:

$$\nu(t) = \nu_0(t) + \Delta\nu_p + \Delta\nu_d e^{-(t-t_g)/\tau_d} + \Delta\dot{\nu}(t - t_g), \qquad (3)$$

where $\nu_0(t)$ is the frequency of the pulsar prior to the glitch occurring at time t_g, $\Delta\nu_p$ is the frequency jump, which is permanent, while $\Delta\nu_d$ is the part that (exponentially) decays at timescale τ_d, and finally $\Delta\dot{\nu}$ specifies the jump in the frequency time derivative. The initial (at time $t = t_g$) frequency jump $\Delta\nu$ is given by $\Delta\nu_p + \Delta\nu_d$.

The frequency behavior prior to and after the glitch (see Figure 6) does not show any recovery term, and therefore we abandon the decaying part of the frequency jump. Assuming that the glitch occurred at the time of the onset of the 2009 January outburst, i.e., MJD 54853.035 (TDB) we derived the following values for the relative frequency jump $\Delta\nu/\nu$ of $(1.9\pm1.6)\times10^{-6}$, and frequency derivative jump $\Delta\dot{\nu}/\dot{\nu}$ of -0.69 ± 0.07. Note that the value for the frequency jump is not significant at face value, in contrast to the frequency derivative jump value of $\Delta\dot{\nu} = +(1.30 \pm 0.14) \times 10^{-11}$ Hz s^{-1}, indicating a dramatic decrease of the spin-down rate. Such an instantaneous decrease in spin-down rate, from $(-18.8 \pm 0.6) \times 10^{-12}$ Hz s^{-1} to

[9] See http://www.atnf.csiro.au/research/pulsar/tempo2.

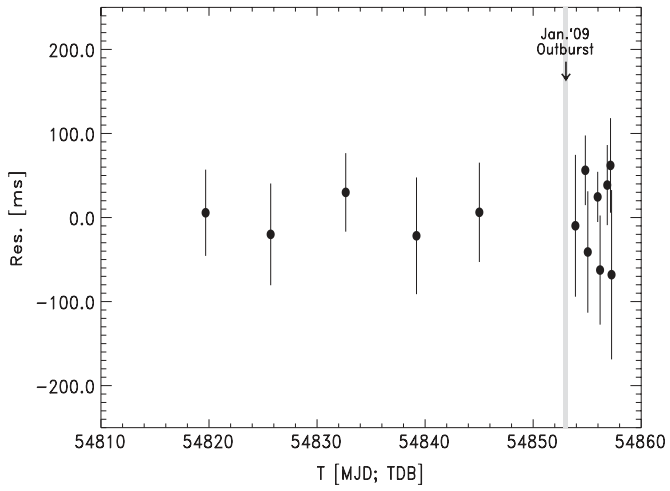

Figure 7. Arrival time residuals (in ms) across the range MJD 54819–54857 for a fit based on a timing model crossing the glitch epoch that was held fixed at the onset of the 2009 January outburst at MJD 54853.035 (TDB).

$(-5.12 \pm 0.02) \times 10^{-12}$ Hz s^{-1}, has not been seen before from any magnetar (see Section 7 for a comparison with earlier reports on magnetar timing).

The arrival time residuals for the best-fitting timing model crossing the glitch, thus including the frequency and frequency derivative jumps, are shown for the range MJD 54819–54857 in Figure 7, and indicate a proper description of the measured ToAs by the glitch-crossing timing model.

3.3.2. 2009 October Glitch

From the middle panel of Figure 1, showing the frequency measurements with superposed the three incoherent timing models, another discontinuity in the timing behavior of 1E 1547.0−5408 can be discerned near MJD 55121 (2009 October 17). Unfortunately, the *RXTE* (and *Swift*) observation sampling is very sparse, such that a detailed study is impossible. From the incoherent models (plus uncertainties; see Table 3) near MJD 55121 we can determine that also for this glitch a strong $\Delta\dot{\nu}/\dot{\nu}$ jump occurred of size (-0.89 ± 0.19), similar to the 2009 January 22 glitch. More surprisingly, in this case the glitch is not accompanied by a radiative outburst (cf. top and middle panels of Figure 1).

3.4. Pulsed Flux Evolution at X-Rays below ∼10 keV

Using either the verified (see Table 4) or non-verified (see Section 3.2.2) coherent timing models we phase-folded barycentered PCA event arrival times according to

$$\Phi(t) = \nu \cdot (t - t_0) + \frac{1}{2}\dot{\nu} \cdot (t - t_0)^2 + \frac{1}{6}\ddot{\nu} \cdot (t - t_0)^3 - \Phi_0 \quad (4)$$

to obtain pulse-phase distributions. $(\nu, \dot{\nu}, \ddot{\nu})$ represent the pulse frequency, first time derivative of the frequency, and second time derivative of the frequency, respectively, while t_0 is the epoch of the ephemeris. Consistent X-ray phase alignment is obtained by subtracting Φ_0 as shown in Equation (4).

Next, for every PCA sub-observation we fitted the pulse-phase distribution, based on events from PCU-2 with PHA values in the range [4,27] (measured energy $\lesssim$10 keV; all Xenon detector layers used), with a model consisting of a constant plus a truncated Fourier series (the fundamental and two harmonics). This yielded for every PCA sub-observation the number of pulsed excess counts which in turn was converted to a (pulsed) count rate using the known exposure time. These PCU-2 (pulsed) count rates for the [4,27] PHA range are shown in the bottom panel of Figure 1 for the time window MJD 54743–55555 (2008 October 3–2010 December 25).

Table 5
Definitions of the *RXTE* Observation Time Segments

Segment No.	Begin/End Date (yyyy-mm-dd)	Start/End (MJD)	Duration (days)	PCU-2/0–4 Exposure (ks)
1	2008-10-03/2008-10-29	54743–54768	26	64.007/116.874
2	2008-11-01/2009-01-14	54771–54845	75	68.783/120.092
3	2009-01-22/2009-02-01	54853–54863	11	84.094/130.199
4	2009-02-06/2009-05-03	54868–54954	87	79.662/149.528
5	2009-05-11/2009-06-22	54962–55004	43	40.614/ 73.717
6	2009-07-14/2009-10-08	55026–55112	87	45.331/ 77.139
7	2009-10-16/2009-12-26	55120–55191	72	47.714/ 81.113
8	2010-01-17/2010-03-09	55213–55264	52	34.472/ 62.683
9	2010-03-17/2010-05-12	55272–55328	57	38.368/ 71.177
10	2010-05-17/2010-07-27	55333–55404	72	45.784/ 83.488
11	2010-08-04/2010-12-25	55412–55555	144	109.704/193.350

Note. PCU-2 and PCU 0–4 exposures are screened adopting default selection criteria, removing short-duration bursts and taking into account detector breakdowns.

If we compare the total and pulsed X-ray flux measurements (both ∼2–10 keV) by *RXTE*/PCA (cf. top and bottom panels of Figure 1), then a completely different evolution is shown, indicating that the pulsed component is (at most) weakly related to the unpulsed or DC component. Most strikingly, the radiative outburst of the pulsed flux in 2008 October is stronger than that in 2009 January, while the total flux outburst in 2009 January is much more intense than that in 2008 October.

Concentrating on the pulsed-flux evolution we note that (1) in 2008 October the pulsed-flux maximum is reached with a delay of about 10 days with respect to the onset of the 2008 October 3 outburst, which is consistent with the findings by Ng et al. (2011) and Scholz & Kaspi (2011), and (2) after the start of the 2009 January 22 outburst the pulsed-flux levels appeared to vary by a factor of ∼2 for about two weeks, then more or less stabilize, and a period of gradual decrease sets in lasting from MJD 54868 up to MJD 55555. Assuming a linear decay over the full period, we find a good reduced χ^2_ν of $66.11/79 = 0.84$ with a best-fit decay rate of $(-6.15 \pm 0.66) \times 10^{-4}$ c (s day)$^{-1}$, estimated for the ∼2–10 keV band of PCU-2, which means a drop of about 54% over the full 688 day period (see the dashed line in the bottom panel of Figure 1).

4. PULSE PROFILE MORPHOLOGY EVOLUTION AT X-RAYS BELOW ∼30 keV

In order to study in detail the evolution of the pulse profile morphology in various X-ray bands, we combined the data from several *RXTE*/PCA sub-observations into 11 time segments spread over the time period from 2008 October 3 up to 2010 December 25 (MJD 54743–55555). Details of these *RXTE* observation time segments can be found in Table 5. The first two time segments refer to *RXTE* observations performed between the 2008 October 3 and 2009 January 22 outbursts, while the other segments have start times beyond the 2009 January 22 outburst (see the middle panel of Figure 1).

After folding each barycentered PCA event time stamp according to Equation (4) from burst and detector breakdown free periods we generated for each of the time segments event

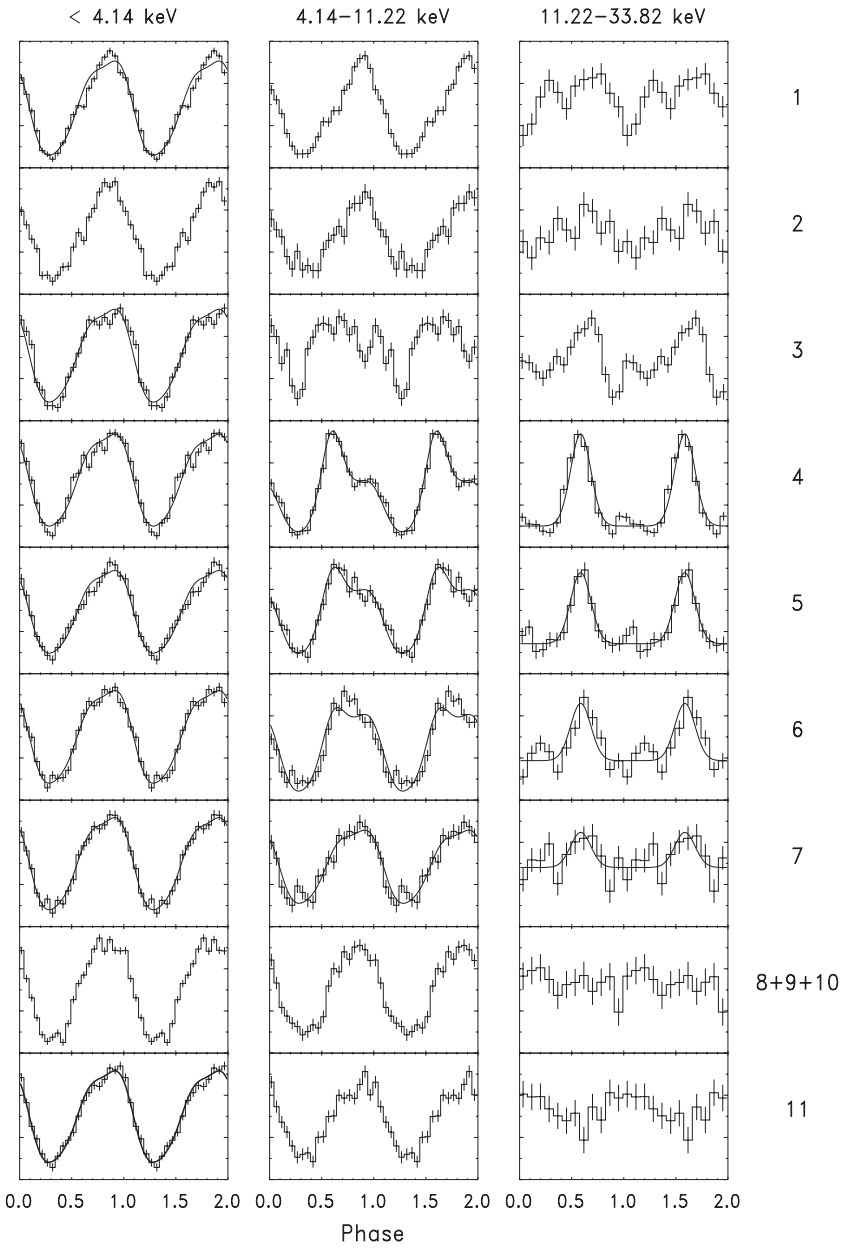

Figure 8. Evolution of the morphology of the (PCA) X-ray pulse profiles in three different energy bands (see headings at the top of the figure). Time-segment identifiers are shown on the right-hand side and are defined in Table 5. In particular, segments 1 and 2 refer to the time period between the 2008 October 3 and 2009 January 22 outbursts. Segment 3 represents a time period of only 11 days in duration starting just after the 2009 January 22 outburst, during which rapid and drastic morphology and flux changes occur.

matrices with (60 × 256) elements by binning the pulse-phase range [0,1] into 60 phase bins for all 256 PHA channels. In this process we used data from *all* three Xenon layers of each PCU, which considerably improves the signal-to-noise ratio for energies above ∼10 keV. This allows us to better characterize the hard X-ray (>10 keV) properties. In Figure 8 the pulse profiles of 1E 1547.0−5408 are shown for all 11 time segments adopting three different X-ray bands: <4.14 keV (soft band, PHA 4–10), 4.14–11.22 keV (medium band, PHA 11–27), and 11.22–33.82 keV (hard band, PHA 28–80). Drastic morphology changes as a function of time are shown for the hard and medium energy bands, especially for the transitions from segment 2 to 3, and 3 to 4. Apparently, the dramatic changes of physical conditions after the 2009 January 22 event (the timing glitch and radiative outburst occur just prior to the start of segment 3) are responsible for these phenomena.

Noteworthy is that the hard X-ray bands of segments 1 and 2 already show pulsed emissions at the 4.7σ and 2.9σ significance levels (applying Z_2^2-tests), respectively. Therefore, the period just after the 2008 October 3 outburst represents the first time period in which pulsed emission from this source has been detected significantly at energies above ∼10 keV.

From Figure 8 it is also clear that the soft X-ray pulse profiles (<4.14 keV) exhibit the least variability and remain relatively stable. This stability was the main reason for choosing the soft X-ray band for the ToA correlation analysis (see Section 3.2.2).

4.1. Evolution of a Transient Hard X-Ray Pulse above ∼10 keV

In the hard X-ray band of segment 4 (see Figure 8, right panel labeled 4) a completely new, relatively sharp, emission feature pops up near phase 0.6 after a short transition phase during

segment 3, which lasts only 11 days. This feature gradually fades and is not detectable anymore beyond segment 7. To obtain the best statistics for this new component in the hard X-ray band we stacked all data from segment 4 up to and including 7, and fitted the resulting pulse phase distribution (in 60 bins) with a model composed of a Gaussian (three free parameters) and a (flat) background (one free parameter). The reduced χ^2_ν of the best fit is $68.21/(60-4) = 1.22$, indicating that the model provides an adequate description of the data. The resulting centroid and width (FWHM $= 2.354\sigma$) of the best-fit Gaussian are 0.587(4) and 0.23(1), respectively.

In order to follow the evolution of the fading hard X-ray pulse, we fitted the hard X-ray pulse profiles of segments 3–11 in terms of this "best-fit" Gaussian (fixed position and width) with free scale and a constant. From the fits we derived the number of excess counts associated with the Gaussian component, which together with the (screened) exposure time for the combination of PCU 0–4 (see the last column of Table 5) can be translated to pulsed count rates.

The quality of the nine fits was good/acceptable except for segments 3 and 4, yielding for both reduced χ^2_ν values of $\sim$1.8 for $60-2 = 58$ degrees of freedom. For segment 4, a slight shift to the left of the Gaussian template provides an excellent fit and a consistent count rate. In the case of segment 3, the observed profile is deviating too much from a Gaussian shape. A fit with a truncated Fourier series (fundamental plus two harmonics) to determine the unpulsed level yielded a good fit (reduced $\chi^2_\nu = 59.54/(60-7) = 1.12$). Now, the pulsed excess counts derived in a phase window [0.426–0.748], centered on 0.587 containing a 90% fraction of the "best-fit" Gaussian, above this differently derived unpulsed level resulted in a pulsed count rate $\sim$1.6 times higher than that estimated by the Gaussian extraction method. Segment 3 seems to represent a transition period starting after the glitch epoch until a configuration/geometry is reached with the relatively narrow hard X-ray pulse at phase $\sim$0.59. In Figure 9 the hard X-ray pulsed count rate, adopting the Gaussian extraction method, is shown versus time since the 2009 January 22 outburst. It is clear that the hard X-ray pulsed component fades to undetectable levels within about 350 days from the onset of the 2009 January 22 outburst.

Also, in spite of the difficulties in reliably estimating the hard X-ray pulsed count rate for segment 3, we can securely state that the maximum emission of the hard X-ray pulsed component is delayed with respect to the 2009 January 22 outburst. This is supported by non-uniformity significance estimations of the pulse phase distributions in the hard X-ray band using Z^2_2 statistics for segments 3 and 4. Although both segments have comparable exposure times (see Table 5), we detect for segment 3 only a 9.2σ pulsed signal, while for segment 4 we find a 27.5σ signal (cf. Figure 8, right panels 3 and 4).

4.2. Modeling the Pulse Profiles below 10 keV

The evolution of the pulse shape in the middle panel of Figure 8 (4.14–11.22 keV band) suggests that the profiles of segments 4 and beyond are composed of two components: (1) a relatively stable one with a shape compatible with that at lower energies (see the left panel of Figure 8) and (2) a transient Gaussian-like feature centered near phase 0.6, the phase of the transient pulse above 10 keV.

In order to model the evolution of the profile shape in the medium band from segment 4 and beyond we now also generated a template for the soft X-ray band (<4.14 keV) using data from the time periods covering segments 8–11, a year after the 2009 January timing glitch. This soft X-ray template has been obtained applying a truncated Fourier series fit, using the fundamental and two harmonics, of the combined <4.14 keV pulse phase distributions of segments 8/9/10 and 11 (see the two lower left panels of Figure 8). The resulting template is superposed on the low-energy pulse phase distribution of segment 11 (see the bottom left corner of Figure 8).

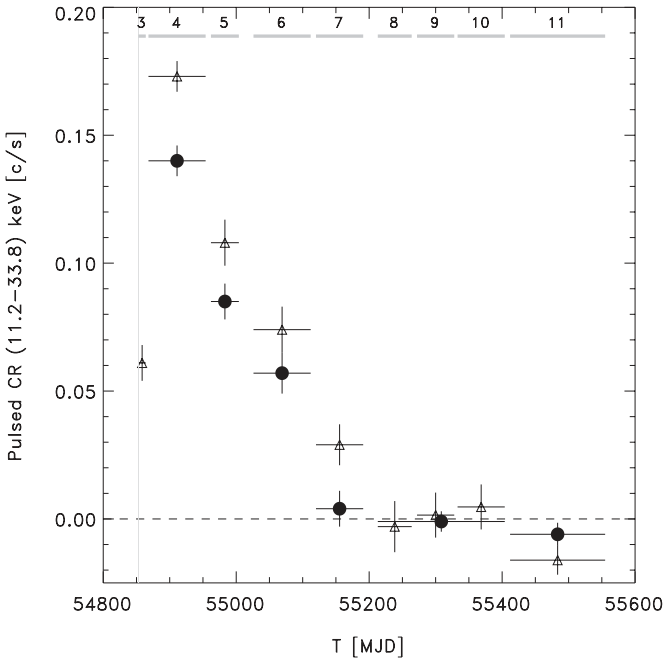

Figure 9. Count-rate evolution since the 2009 January 22 outburst (shown as a vertical gray line) of the transient hard X-ray pulse (triangles) for energies $\sim$11.2–33.8 keV (see Section 4.1). The selected PCA time segments are indicated near the top of the figure. The hard pulsed component reaches its maximum in segment 4, which starts 15 days after the onset of the 2009 January 22 outburst and lasts 87 days. Next, this component fades to undetectable levels within $\sim$350 days from the onset. The fading trend of this component is also clearly visible at lower energies ($\sim$4.1–11.2 keV; dots). All errors are statistical only (1σ).

Next, we fitted all <4.14 keV pulse phase distributions in terms of a constant and the soft X-ray template with free normalization, and obtained good/reasonable (even for segment 3) fits for all segments except 1 and 2 (most of the fits are superposed on the distributions shown in the left panel of Figure 8). Therefore, we conclude that the pre-2009 January 22 outburst soft X-ray profile differs significantly from that of the post-2009 January 22. The post-outburst model clearly underestimates the pulsed emission near the maximum and overestimates the contribution near phase 0.6 (see the top left panel of Figure 8).

Finally, the medium-energy profiles from segments 4 and beyond were fitted with a model composed of a constant, the soft X-ray and hard X-ray (Gaussian) templates both with free scale. We obtained acceptable fits, i.e., $\chi^2_\nu \lesssim 1.36$ for 57 degrees of freedom, for all time segments except for segment 6 ($\chi^2_\nu \simeq 1.82$). From the scale factors of the best fits and exposure times, the count rates for both the soft X-ray and hard X-ray components can be determined. For the hard X-ray (Gaussian) component these rates are added in Figure 9, and show a similar fading trend as visible at higher X-ray energies, meaning that the hard Gaussian-like transient pulse extends toward lower X-ray energies. For segment 4 $38\% \pm 2\%$ of the total pulsed emission in the medium-energy band can be attributed to the hard X-ray

Gaussian component, while for segments 5 and 6 these numbers are 24% ± 2% and 15% ± 2%, respectively.

5. BROADBAND SPECTRAL EVOLUTION: TOTAL AND PULSED X-RAY EMISSIONS UP TO ∼300 keV

For our spectral analyses of the total and pulsed emissions, we addressed the broad energy range from ∼1 keV up to ∼300 keV, exploiting the different capabilities of instruments on board three high-energy observatories: *RXTE*, *Swift*, and *INTEGRAL*. Data from the non-imaging *RXTE* instruments PCA and HEXTE have been used to obtain spectral information on the pulsed emission over a broad energy range, ∼2.5–250 keV, while data from the *Swift*/XRT instrument in the PC mode have been analyzed to derive the total emission spectrum at soft X-rays (0.2–10 keV). Using *INTEGRAL*/ISGRI data spectral information has been obtained for both the total and pulsed emission of 1E 1547.0−5408 over the 20–300 keV energy band. Finally, during the early phase of the decay of the 2009 January outburst JEM-X1 (3–30 keV) detected 1E 1547.0−5408 up ∼15 keV, and through imaging analysis spectral information of the *total* emission could even be obtained for energies between 10 and 15 keV, a range not/hardly accessible for other high-energy instruments with imaging capabilities.

All our spectral results have been corrected for interstellar absorption adopting a hydrogen column density $N_{\rm H}$ of 3.12×10^{22} cm^{-2} (see, e.g., Gelfand & Gaensler 2007; Halpern et al. 2008, slightly above the total Galactic H I column density estimated to be in the range $(1.81–2.25) \times 10^{22}$ cm^{-2}), and thus correspond to unabsorbed source spectra. Note that these corrections are only effective for photon energies below ∼5 keV, and thus it is not necessary to apply these to HEXTE and ISGRI data.

5.1. RXTE/PCA and HEXTE Pulsed X-Ray Spectra

Analogous to the procedure followed for the PCA to obtain event matrices (see Section 4) we generated for the HEXTE data for all 11 time segments two-dimensional (burst-free) event distributions sorting on pulse phase and energy. First, we verified that for the combined *RXTE* time segments 4–7 we also detect with HEXTE at hard X-rays the same Gaussian-shaped high-energy pulse as measured with the PCA below ∼30 keV. Figure 10 shows the HEXTE pulse profiles for the energy bands 32.1–60.1 keV and 60.1–156.6 keV in which this Gaussian profile is found at the same pulse phase, with non-uniformity significances 10.6σ and 8.9σ, respectively.

Next, we derived pulsed excess counts in user-selected energy (PHA) bands for both PCA and HEXTE data by fitting a truncated Fourier series (using the fundamental plus two harmonics) to the pulse-phase distributions measured in these bands. The fit function minimum plus associated error are used to determine the number of pulsed excess counts, i.e., the number of counts above this minimum (=unpulsed, i.e., DC plus background level) for each user-selected energy band.

For the PCA we constructed time-averaged energy response matrices for each PCU separately taking into account the different (screened) exposure times of the involved PCUs during the time period of interest. For this purpose we used the *ftools* version 6.4 programs *pcarsp* and *addrmf*. To convert PHA channels to measured energy values, $E_{\rm PHA}$, for PCU combined/stacked products we also generated a weighted PCU-combined energy response matrix.

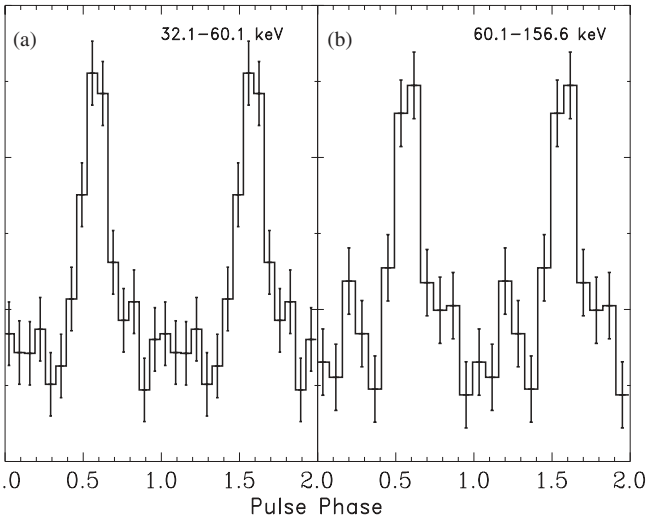

Figure 10. HEXTE pulse profiles for the 32.1–60.1 keV (10.6σ; panel (a)) and 60.1–156.6 keV (8.6σ; panel (b)) bands combining data from *RXTE* time segments 4–7. The Gaussian-shaped hard X-ray profile extends up to ∼150 keV.

For HEXTE we employed cluster A and B energy-response matrices separately, taking into account the different screened on-source exposure times and the reduction in efficiency in case of off-axis observations. The on-source exposure times for both clusters have been corrected for the considerable dead-time effects.

To translate the derived pulsed excess counts to photon flux values we employed these response matrices in (forward folding) spectral fitting procedures adopting simple underlying photon emission models such as a power law, a combination of two power laws, or a power law plus an (exponential) cutoff power law.

The results of the spectral fits to the combined PCA/HEXTE data sets[10] for the pulsed emission of all 11 segments along with the (reconstructed) flux measurements are shown in a νF_ν representation in Figure 11 for the range ∼2.5–150 keV. In this figure the HEXTE results for segments 1, 2, and 11 are left out for clarity because the non-detections in the different energy bands correspond to 2σ upper-limit levels comparable to those shown for segments 8/9/10. However, HEXTE did detect pulsed emission (3.6σ) in its integral energy band, ∼15–250 keV, for segment 1, confirming the PCA findings (see Section 4).

Below ∼10 keV the pulsed spectra are all, irrespective of the time segment, very soft with photon indices Γ in the range −[3.9–4.2] (except for segment 3, $\Gamma \simeq -4.6$). Also, a significant decrease by a factor of ∼2 in normalization is shown for the time period between the two outbursts, moving from segment 1 to 2. Then, promptly after the 2009 January outburst a strong increase in normalization by a factor of ∼2 is observed, moving from segment 2 to 3, followed by a gradual decrease down to the level shown for segment 11. The whole picture for energies below ∼10 keV is consistent with the behavior in the coarse (∼2–10 keV) energy band shown in the bottom panel of Figure 1.

Above ∼10 keV the variations are more drastic. Since the initial activation of pulsed high-energy emission after the 2008 October outburst this component reached undetectable

[10] We applied the following energy-independent normalization factors of 0.912 (PCA) and 1.087 (HEXTE) to the spectral measurements in order to obtain consistent high-energy Crab pulsed fluxes (see Section 3.4 of Kuiper et al. 2006).

Table 6
Characteristics of the Spectral Fits, Adopting a Combination of a Power Law and a Cutoff Power Law[a], to *RXTE*/PCA and HEXTE (2.5–150 keV) *Pulsed* Flux Data

RXTE Segm.	E_0 (keV)	k_1[b] ($\times 10^6$)	Γ_1	k_2[b] ($\times 10^5$)	Γ_2	E_c (keV)	F_E^{2-10}[c]	F_E^{20-150}[c]
3	12.9295	1.10 ± 0.11	$-4.63^{+0.08}_{-0.07}$	1.49 ± 0.32	$+0.37^{+0.20}_{-0.28}$	44.0 ± 10.4	$1.47^{+0.06}_{-0.07}$	$6.9^{+1.2}_{-1.0}$
4	12.8760	2.68 ± 0.21	$-3.92^{+0.06}_{-0.06}$	1.86 ± 0.33	$+0.59^{+0.19}_{-0.25}$	33.8 ± 5.9	$1.28^{+0.04}_{-0.05}$	$7.5^{+0.9}_{-1.0}$
5/6/7	12.8875	2.50 ± 0.15	$-3.92^{+0.05}_{-0.05}$	0.43 ± 0.15	$+1.55^{+0.26}_{-0.42}$	25.3 ± 4.8	$1.18^{+0.03}_{-0.04}$	$4.1^{+0.9}_{-0.9}$

Notes. Quoted errors are for a 68.27% confidence level (1σ).
[a] The (photon flux) fit model is $F_\gamma(E_\gamma) = k_1 \cdot (E_\gamma/E_0)^{\Gamma_1} + k_2 \cdot (E_\gamma/E_0)^{\Gamma_2} \cdot \exp(-E_\gamma/E_c)$.
[b] The normalizations k_1 and k_2 are in units ph cm^{-2} s^{-1} keV^{-1} at pivot energy E_0.
[c] The unabsorbed energy fluxes F_E^{2-10} and F_E^{20-150} are in units 10^{-11} erg cm^{-2} s^{-1}.

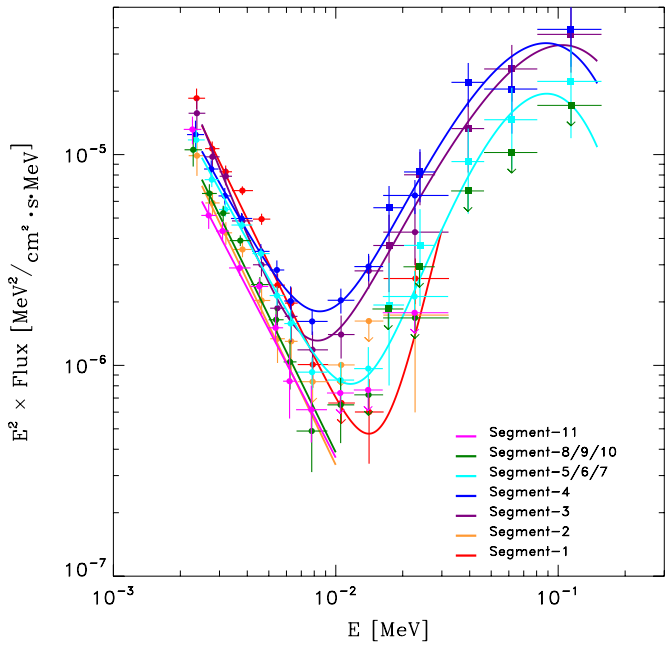

Figure 11. Spectral evolution from 2008 October to 2010 December of the pulsed (unabsorbed) emission of 1E 1547.0−5408 in the 2.5–150 keV band as measured by *RXTE*/PCA (filled circles) and HEXTE (filled squares) for time segments 1–11 (see Table 5 and the middle panel of Figure 1). Power-law plus cutoff power-law-model fits are superposed for segments 3, 4, and 5/6/7 (see Table 6), during which significant pulsed emission was detected by HEXTE above ∼15 keV, otherwise only power-law-model fits are shown below 10 keV. The pulsed hard X-ray emission ($\gtrsim$10 keV) becomes maximal during segment 4, showing therefore a delayed increase with respect to the onset of the 2009 January outburst, before a gradual decline sets in.

levels during segment 2, but increased dramatically after the 2009 January outburst, reaching eventually a maximum during segment 4, after which a gradual decrease sets in resulting to undetectable levels beyond segment 7.

During the periods with significant pulsed hard X-ray emission the best spectral description over the full 2.5–150 keV band consists of a combination of a power-law plus a cutoff power-law model (see Table 6 for quantitative information). The improvement relative to a model composed of two power laws is about 3.5σ, considering the combination of the three periods, segments 3, 4, and 5/6/7, during which significant pulsed hard X-ray emission has been detected.

For the cutoff power-law model component, $F(E_\gamma) = k \cdot (E_\gamma/E_0)^\Gamma \cdot \exp(-E_\gamma/E_c)$ with k the normalization in ph cm^{-2} s^{-1} keV^{-1}, E_0 the pivot energy, Γ the power-law (photon) index, and E_c the cutoff energy, the photon index at a specific energy $\Gamma^* := (d \ln F)/(d \ln E_\gamma)$ is given by $\Gamma^* = \Gamma - E_\gamma/E_c$. Therefore, for this model component the maximum in a νF_ν spectral representation (maximum power per energy decade) is found at $E_\gamma^{\max} = (\Gamma+2) \cdot E_c$. For the spectral fits of segments 3, 4, and 5/6/7 the best-fit parameters for Γ and E_c yield νF_ν maxima for energies in the range 90–105 keV with an uncertainty of about 20 keV. We stress that our data do not constrain the extrapolation of the spectra, the spectral shape, above these energies.

1E 1547.0−5408 exhibits in time segment 4, extending over 87 days, the maximal pulsed flux at energies above 10 keV. An important parameter for theoretical modeling is the time between the onset of the outburst/timing glitch and the epoch at which the maximal flux of the non-thermal transient component is reached. We used the high count rate in the *RXTE*/PCA to divide segment 4 in three time intervals to study the spectral evolution in more detail. The normalization of the spectra appeared maximal in two intervals between 37 and 101 days after the onset of the 2009 January outburst. We refer to this delay as 70 ± 30 days.

5.2. *Swift*/XRT Soft X-Ray Spectra of the Total Emission

To study the evolution of the *total* (=pulsed plus unpulsed) emission spectrum of 1E 1547.0−5408 at soft X-rays (0.5–10 keV) since the 2009 January outburst we used *Swift*/XRT data obtained in the PC mode, allowing full two-dimensional imaging information (see Section 2.3). This information is necessary to get rid of the emission from the dust scatter rings (Tiengo et al. 2010) which were prominently present during the early part of the decay phase after the 2009 January outburst.

The *Swift* observations selected for this analysis are chosen such that these cover (sometimes approximately) time periods for which hard X-ray *INTEGRAL* observations have been performed (see Table 2 and Section 2.3 for the *INTEGRAL* and *Swift* observations, respectively), supplemented with some recent observations (e.g., those with observation identifiers 00090404019, 2010 September 28, and 00090404027, 2011 February 25) to follow the late-time evolution.

We selected events from a 60″ circular aperture centered on 1E 1547.0−5408 using (default) cleaned event lists. For this selection we executed procedure `xrtmkarf` (version 0.5.8 embedded in the `HEASOFT` instrument specific software analysis environment) to obtain appropriate sensitive area information, stored in so-called ancillary response files (arf), which takes into account the reduction in sensitive area for off-axis observations and the finite angular size of the source extraction region (about 90% of the source counts fall within a 60″ circle centered on the source). The energy redistribution matrix (rmf) used was `swxpc0to12s6_20070901v011.rmf`.

Table 7
Characteristics of the Spectral Fits, Adopting a Combination of a Power Law and a Blackbody,[a] to Solely *Swift*/XRT-PC (0.5–10 keV) *Total* Flux Data

Swift/XRT Obs.	Date	MJD Range	kT (keV)	Γ	F_E^{1-10b} (Pl-model)	F_E^{1-10b} (BB-model)	Color in Figure 13
00030956034	2009 Jan 29	54860.005–54860.343	0.606 ± 0.007	-1.14 ± 0.04	5.07 ± 0.50	4.48 ± 0.32	Orange
00030956039	2009 Feb 4	54866.702–54866.974	0.564 ± 0.006	-1.32 ± 0.04	4.41 ± 0.37	4.26 ± 0.31	Purple
00030956051	2009 Aug 19	55062.069–55062.150	0.775 ± 0.018	-1.99 ± 0.16	1.71 ± 0.45	2.52 ± 0.36	Dark blue
00090404003	2010 Apr 12	55298.509–55298.938	0.728 ± 0.014	-2.84 ± 0.20	0.93 ± 0.22	1.36 ± 0.16	Aqua

Notes. The Γ values change when the *INTEGRAL* flux values above 20 keV are included in the fits (see Table 8). Quoted errors are for a 68.27% confidence level (1σ).
[a] The (photon flux) fit model is $F(E_\gamma) = \alpha_{\rm bb} \cdot E_\gamma^2/(\exp(E_\gamma/kT) - 1) + \alpha_{\rm pl} \cdot E_\gamma^{\Gamma}$.
[b] The energy fluxes F_E^{1-10} are unabsorbed ($N_{\rm H} = 3.12 \times 10^{22}$ cm^{-2}) and in units 10^{-11} erg cm^{-2} s^{-1} for the 1–10 keV band.

We also selected a background region composed of an annular region with a 180″ inner radius and 240″ outer radius centered on 1E 1547.0−5408, seven times larger than the source region. From this we estimated the number of background counts in our source region, which was $\lesssim$1% of the total number of counts confined in our source region, and therefore no background correction has been made in subsequent spectral fitting procedures.

Sorting the selected (source region) events on energy we fitted the resulting event distribution in measured energy space to a certain model photon spectrum attenuated by interstellar absorption (see Section 5) in a forward folding procedure using the appropriate response information (`arf` and `rmf` response files). As model (source) spectrum a combination of a BB and Pl was used which can adequately reconstruct (empirically) the measured spectral distributions below 10 keV. These model fits were also successfully applied and discussed for 1E 1547.0−5408 by, e.g., Gelfand & Gaensler (2007), Ng et al. (2011), Bernardini et al. (2011), and Scholz & Kaspi (2011).

The spectral fit parameters adopting this composite BB+Pl model are given in Table 7 and the flux measurements for the 0.5–10 keV range reconstructed from spectral fits are shown in Figure 13. Energy fluxes provided in Table 7 are unabsorbed and specified for the 1–10 keV band to facilitate comparisons with the results of Scholz & Kaspi (2011). All fits have acceptable reduced χ^2 values near 1 assuming a fixed $N_{\rm H}$ of 3.12×10^{22} cm^{-2}. The fit values for the BB temperature kT and Pl index Γ as a function of time since the start of the outburst are consistent with those reported by, e.g., Bernardini et al. (2011) and Scholz & Kaspi (2011). Table 7 also confirms a clear softening of the Pl index with time and a decreasing flux below 10 keV (also visible in the spectral shapes below 10 keV in Figure 13). This hardness–intensity correlation has been discussed previously, e.g., by Scholz & Kaspi (2011); however, our spectral fits to the combined *Swift–INTEGRAL* spectra over the broad energy band 1–300 keV provide a different, alternative decomposition and hardness–intensity correlation (Section 5.4).

5.3. *INTEGRAL* Soft γ-Ray Total Emission Spectra

The ISGRI observations (science windows) selected for our study all have observation dates between 2008 October 3 and 2010 April 3 and instrument pointings within 14.°5 from the 1E 1547.0−5408 sky location. This ensures that (a part of) the detector plane is illuminated by the target. The resulting list is further screened on erratic count rate variations, indicative for particle-induced effects due to Earth-radiation-belt passages or solar-flare activities, by inspecting visually the count rate in 20–30 keV band versus time. Science windows showing erratic count-rate variations are excluded for further analysis. Moreover, we ignored time intervals during which bursts (from any source in the field of view) occurred. This selection is particularly important for *INTEGRAL* revolutions 767–772 during which copious numbers of bursts from 1E 1547.0−5408 have been detected. The set of *INTEGRAL* revolutions used along with the effective on-axis exposure times is given in Table 2.

The *total* emission spectrum at soft gamma-rays/hard X-rays above 20 keV can be derived by exploiting the arcminute imaging capability of ISGRI. We generated sky maps for each selected science window (see Section 2.2) in different energy bands covering the 20–300 keV energy window. From these maps sky mosaics were assembled using dedicated imaging software tools embedded in the OSA 7.0 analysis environment. We chose in most cases a logarithmically binned energy grid with 10 bins covering the 20–300 keV range, but also 4 logarithmic energy bins over the 20–150 keV range when we expected low flux levels for 1E 1547.0−5408 (e.g., for *INTEGRAL* Revs. 899–912). The final product of the imaging analysis provides the count rate, its variance, exposure, and significance for all energy bands over the (deconvolved) mosaicked sky field. As an example Figure 12 shows the significance map (20–150 keV) in a wide field centered on 1E 1547.0−5408 combining observations from *INTEGRAL* Revs. 899–912, performed more than a year after the 2009 January outburst. 1E 1547.0−5408 is clearly detected in this mosaic at a level of $\sim 9.5\sigma$.

The total emission spectrum of 1E 1547.0−5408 can be derived from the count-rate and variance maps by extracting the (dead-time-corrected) rates and uncertainties at the location of 1E 1547.0−5408. These values are normalized to the count rates measured for the total (nebula and pulsar) emission from the Crab in similar energy bands, using Crab calibration observations (in 5×5 dither mode) performed during *INTEGRAL* Rev. 102. From the ratios and the photon spectrum of the total emission from the Crab, we can derive the total high-energy photon spectrum of 1E 1547.0−5408 (pulsed and any unpulsed point-source component). For the total Crab photon spectrum we used the broken-power-law spectrum derived by Jourdain & Roques (2008) based on *INTEGRAL*/SPI observations of the Crab at energies between 23 and 1000 keV. The latest Crab cross calibrations between SPI and IBIS-ISGRI provided consistent results.

Figure 13 shows the ISGRI flux measurements (20–300 keV) for different sets of observations performed between 2009 January 24 and 2010 April 3 (Revs. 767–912; see Table 2). For the (only) 100 ks ToO observation performed during 2008 October 8–10 (Rev. 731; a couple of days after the 2008 October 3 outburst) no significant flux values can be derived with 2σ upper limits (not shown in Figure 13) consistent with the pulsed-flux detections by *RXTE*/PCA and HEXTE.

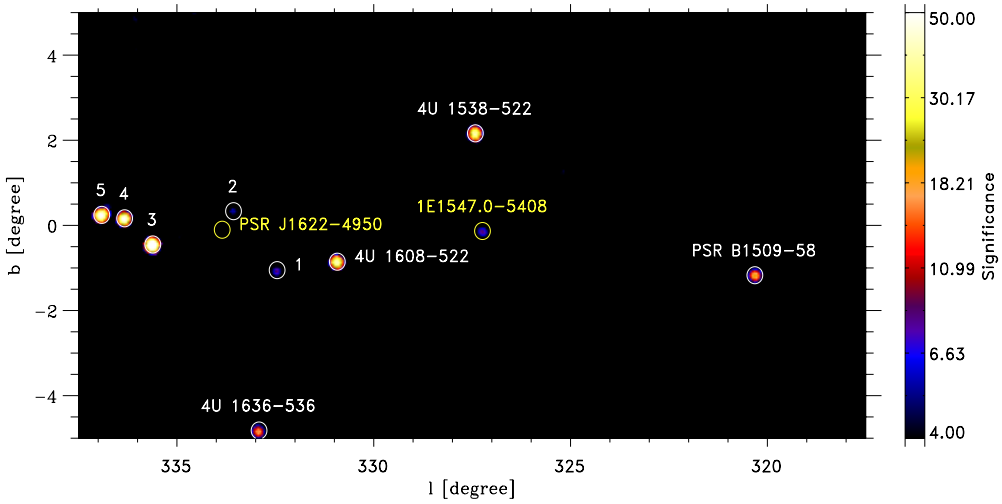

Figure 12. *INTEGRAL*/ISGRI significance map for the 20–150 keV band of a 20° × 10° field centered on 1E 1547.0−5408 based on observations performed during *INTEGRAL* Revs. 899–912 (2010 February 23–April 3), more than a year after the 2009 January outburst. The effective exposure on 1E 1547.0−5408 is ∼717.7 ks, and its detection significance is still 9.5σ. The location of another radio-loud magnetar, PSR J1622−4950, not detected by *INTEGRAL*, is also indicated by a yellow circle. Other high-energy sources detected by ISGRI during Revs. 899–912 are indicated either by name or number. Those labeled with a number are (1) IGR J16207−5129, (2) AX J1619.4−4945, (3) IGR J16318−4848, (4) AX J1631.9−4752, and (5) 4U 1636−536.

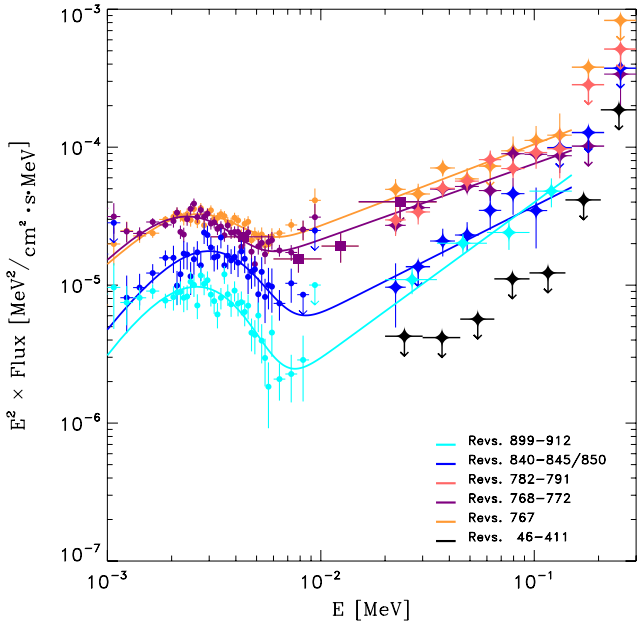

Figure 13. Spectral evolution after the timing glitch/outburst in 2009 January up to 2010 April of the total (unabsorbed) emission of 1E 1547.0−5408 in the 1–300 keV band as measured by *Swift*/XRT (PC mode; filled circles), *INTEGRAL* JEM-X (filled squares), and ISGRI (filled diamonds). BB plus Pl-model fits for the combined fluxes are shown. The different colors indicate the *INTEGRAL* observations (revolutions) with (nearly) contemporaneous *Swift* observations. Note that for the period covering Revs. 782–791 no XRT observations have been performed in the PC mode. Black 2σ upper limits are shown for the combined exposure of ∼4 Ms of all *INTEGRAL* observations (prior to the 2008 October outburst) from 2003 March to 2006 February.

We added in Figure 13 also the 2σ upper limits on the 1E 1547.0−5408 flux derived from a deep 4 Ms mosaic (see, e.g., Kuiper et al. 2008) using *INTEGRAL* observations performed between Revs. 46 and 411 (2003 March 2–2006 February 24) targeting on PSR J1617−5055, which is located within 5.°5 from 1E 1547.0−5408. These upper limits are at least 10 times lower than the flux levels reached during *INTEGRAL* Revs. 767–791 in which the hard spectral tail is detected most significantly.

During the intensive monitoring campaign (Revs. 767–772) of 1E 1547.0−5408 the source was also for ∼264.8 ks within 3.°75 of the JEM-X1 pointing axis. In the combination of these observations JEM-X1 clearly detected 1E 1547.0−5408 at a 8.6σ level between 3.04 and 15.04 keV. Flux values are obtained using similar procedures as applied for ISGRI, i.e., count rates are expressed in Crab (total) flux units and subsequently converted to flux units; however, now we have to take into account the different column densities along the line of sight for the Crab ($N_{\rm H}$ of 3.2×10^{21} cm^{-2}) and 1E 1547.0−5408 ($N_{\rm H}$ of 3.12×10^{22} cm^{-2}). The four JEM-X1 flux measurements (three detections and one upper limit) are shown in Figure 13 as filled squares.

5.4. INTEGRAL and Swift/XRT Total-emission Spectral Evolution

To extend the spectral coverage down to ∼1 keV we combined the ISGRI/(JEM-X1) observations with the (nearly) contemporaneous *Swift*/XRT observations performed in the PC mode (see Section 5.2). This allowed us to study the spectral shape and spectral evolution over the broad 1–300 keV interval. We found that a fit with a BB plus (single) Pl model to the flux measurements over the total energy range provided a statistically good fit. No fudge factors were used in these fits to absorb calibration uncertainties between different instruments. The model fits are shown in Figure 13. The spectra of the two late-time *Swift*/XRT observations of 2010 September 28 and 2011 February 25 are not shown for clarity because these are fully overlapping with the spectrum (aqua-colored) of the observation performed on 2010 April 12 slightly after *INTEGRAL* Revs. 899–912.

Characteristics of these XRT/ISGRI combined spectral fits are listed in Table 8. The first thing to note is that also for this broad energy band two spectral components, a BB plus a Pl model, appear to be sufficient to fit the flux values (see also Bernardini et al. 2011). The fit values for the BB temperature kT (Table 8) are close to those derived for solely 0.5–10 keV band *Swift*/XRT data (Table 7); however, the Pl photon indices Γ in the third column of Table 8 are very different, ranging from ~ -1.4 after the 2009 January glitch/outburst to ~ -0.9 almost 14 months later, while the 20–150 keV flux is fading

Table 8
Spectral Properties of the *Total* Emission of 1E 1547.0−5408 across the 1–300 keV Range for Various *INTEGRAL* Observation Periods (Orbital Revolution Numbers, See Table 2)

INTEGRAL Obs. Period	Flux (20–150 keV)	Γ	*kT* (keV)	BB-Flux[a] (2–10 keV)	Pl-Flux[a] (2–10 keV)
767	(2.52 ± 0.37)E−10	−1.41 ± 0.06	0.621 ± 0.008	(2.51 ± 0.22)E−11	(4.49 ± 0.23)E−11
768–772	(1.85 ± 0.18)E−10	−1.45 ± 0.04	0.566 ± 0.007	(2.35 ± 0.19)E−11	(3.66 ± 0.17)E−11
782–791[b]	(2.15 ± 0.14)E−10	−1.27 ± 0.11	...	...	...
840–850	(0.84 ± 0.27)E−10	−1.22 ± 0.10	0.739 ± 0.014	(2.23 ± 0.27)E−11	(0.91 ± 0.17)E−11
899–912	(0.80 ± 0.22)E−10	−0.87 ± 0.07	0.654 ± 0.010	(1.18 ± 0.11)E−11	(0.35 ± 0.06)E−11
46–411[b,c]	<0.15E−10	−1.35 (fixed)	...	...	...

Notes. After the timing Glitch in 2009 January, derived by fitting a blackbody plus power-law model to (nearly) contemporaneous *INTEGRAL*/ISGRI and *Swift*/XRT data. *INTEGRAL* Revs. 46–411 represent a total of 4 Ms of observations of 1E 1547.0−5408 before 2006 March.
[a] All fluxes are unabsorbed adopting $N_H = 3.12 \times 10^{22}$ cm^{-2} and in units erg cm^{-2} s^{-1}.
[b] Only ISGRI data used adopting the power-law model.
[c] Upper limit at 2σ confidence.

by a factor of ∼3. In agreement with this, den Hartog et al. (2009), using ∼200 ks of *INTEGRAL* (near real time) ToO data taken 2–8 days after the 2009 January glitch/outburst, and Enoto et al. (2010a), using *Suzaku* data taken ∼7 days after the 2009 January glitch/outburst, consistently reported a power-law index of ~ -1.5 during the first half of *INTEGRAL* observation period Revs. 767–772 (see Table 1). Furthermore, Enoto et al. (2010a, *Suzaku* data) and Bernardini et al. (2011, *Chandra* and *INTEGRAL* data) also derived for energies ∼0.5–100 keV within statistical uncertainties the same fit result as given in Table 8 for epochs in *INTEGRAL* Revs. 767–772. Thus, the power-law component resulting from the fits below 10 keV is not required when the broad energy range is considered. The "new" hard power-law component explains the total hard X-ray emission above ∼10 keV and also contributes significantly to the emission below 10 keV. Moreover, the index is hardening with decreasing flux, the opposite trend to what is visible in Table 7 and discussed in, e.g., Scholz & Kaspi (2011) for spectral fits restricted to energies below 10 keV.

The fading trends of the total fluxes at soft X-rays and hard X-rays since the 2009 January outburst are shown in Figure 14. The total (unabsorbed) soft X-ray flux is the sum of the BB and Pl components (last two columns of Table 8). The power-law contribution at soft X-rays is negligible after 2010 April 12. Namely, late-time *Swift*/XRT measurements of the total soft X-ray spectrum of 1E 1547.0−5408 demonstrate that a single BB component is sufficient to describe the spectrum adequately. The (late-time) flux measurements of *Swift* observations 0009040419 (2010 September 28) and 00090404027 (2011 February 25) are added in Figure 14. The corresponding (unabsorbed) 2–10 keV fluxes and temperatures are $(1.67(9) \times 10^{-11}$ erg cm^{-2} s^{-1}, $kT = 0.671(5))$ and $(1.06(7) \times 10^{-11}$ erg cm^{-2} s^{-1}, $kT = 0.600(6))$, respectively.

It is evident from Figures 13 and 14 that the total source fluxes are maximal during the first *INTEGRAL* ToO observation after the 2009 January glitch/outburst epoch (Rev. 767, starting two days after the 2009 January outburst) for energies below 10 keV as well as for the soft gamma-rays/hard X-rays (20–150 keV). It is remarkable that for the latter *total* non-thermal emission we do not see evidence that maximal luminosity is reached about 70 ± 30 days after the glitch (in *RXTE* and *INTEGRAL* segments 4), a behavior we found for the transient *pulsed* component for energies above ∼20 keV. Apparently, the increase of the *pulsed* emission above 20 keV is delayed with respect to that of the unpulsed emission above 20 keV. The contribution of the pulsed

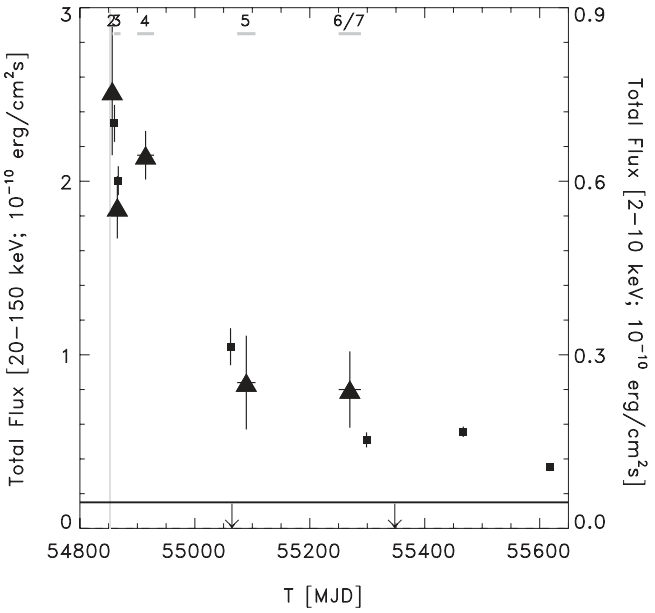

Figure 14. Evolution of the total (unabsorbed) energy flux of 1E 1547.0−5408 since the 2009 January outburst in two different energy bands: 2–10 keV (*Swift*/XRT; solid squares; right flux scale) and 20–150 keV (ISGRI; filled triangles; left flux scale). The onset of the 2009 January outburst is indicated by a vertical line, and the *INTEGRAL* observation segments (see Table 2) are shown in the top part of the figure. The horizontal line represents the 2σ upper limit for the 20–150 keV flux as derived from *INTEGRAL* observations performed during Revs. 46–411 (before 2006 March).

component to the total flux (=pulsed fraction) in the 20–150 keV band during *INTEGRAL* segment 4 amounts to 34%±9%. At the start of the 2009 January outburst this fraction was 31% ± 7%, and about 240 days later during *INTEGRAL* segment 5 it was 45% ± 14%.

6. SUMMARY

In this paper we presented new and detailed characteristics of the persistent (non-burst) emission of 1E 1547.0−5408 between ∼1 and 300 keV analyzing data collected over a period of 27 months, starting with the onset of an outburst in 2008 October, covering the epoch of the 2009 January outburst, and ending two years later in 2011 January. Detailed results are derived on the timing characteristics, the evolutions of the total and pulsed persistent emissions, and pulse profiles. In particular, the evolution of the total and pulsed emission of a magnetar for

energies above ∼10 keV after the event of a major timing glitch accompanied with a radiative outburst has been revealed for the first time. We used *RXTE*/PCA and *Swift*/XRT monitoring data to derive incoherent and coherent timing models for the pulse frequency evolution between 2008 October and 2011 January. *RXTE*/PCA and HEXTE data were used to derive the evolution of the pulse profile, flux, and spectrum of the pulsed emission from ∼2.5 to 150 keV. Finally, we exploited the imaging capabilities of *Swift*/XRT and *INTEGRAL*/ISGRI to derive the evolution of the flux and spectra of the *total* emission for energies from ∼1 to 300 keV after the 2009 January outburst. What follows is a summary of the main results.

6.1. Total Flux Evolution of 1E 1547.0−5408 below 10 keV

1. Using *RXTE*/PCA data we derived the total flux evolution for energies ∼2–10 keV from 2008 October 3 up to 2010 December 25 showing the outburst in 2008 October and the much more intense outburst in 2009 January. The flux decay of the latter has still not reached its quiescent level ∼2 years after the outburst (see Section 3.1 and the upper panel of Figure 1). See also Israel et al. (2010), Bernardini et al. (2011), and Scholz & Kaspi (2011).
2. We can satisfactorily describe the decay of the total flux after the intense 2009 January 22 (MJD 54853.911) outburst with a rapidly decaying power-law component, dominating only during a period of ∼5 days after the outburst, and a slowly decaying exponential component with a typical timescale of ∼200 days (Section 3.1).
3. In the tail of the intense 2009 January 22 outburst we detected two mini-outbursts, at MJD 54920 and at MJD 55207, with enhanced emission over periods of ∼450 s and ∼130 s, respectively, and superposed with short-duration bursts. In the tail of the latter outburst we found in a time window of only 52 s a pulsed signal (energies ∼2–20 keV) of ∼13 σ significance (Section 3.1.1). The latter event might be similar to the persistent, pulsed emission enhancement reported by Kaneko et al. (2010) using *Fermi*/GBM for a time interval just after the onset of the 2009 January outburst of 1E 1547.0−5408.

6.2. Evolution of the Pulse Frequency of 1E 1547.0−5408 and Glitch Detections

1. From a timing analysis of *RXTE*/PCA sub-observations we derived the evolution of the pulse frequency from 2008 October 3 until 2010 December 25, based on incoherent measurements (see Section 3.2 and the middle panel of Figure 1).
2. Two apparent discontinuities in the pulse-frequency evolution are visible, near MJD 54853 (the onset of the 2009 January 22 outburst) and near MJD 55121 (2009 October 17). For three time intervals, before, between, and after the epochs of these timing discontinuities, we derived simple incoherent timing models (Taylor series) with either three or four timing parameters (ν, $\dot{\nu}$, $\ddot{\nu}$, [$\dddot{\nu}$]; Section 3.2.1 and Table 3).
3. Phase-coherent timing models have been constructed for six time intervals, each of duration ∼30–35 days, using *RXTE*/PCA and *Swift*/XRT overlapping observations. Most importantly, one phase-connected ephemeris was derived after the onset of the 2008 October outburst (see also Ng et al. 2011 and Israel et al. 2010), and one just before the 2009 January outburst and two directly after this second outburst (Section 3.2.2 and Table 4).
4. Applying standard glitch fitting techniques we measured at the time of the onset of the 2009 January outburst (i.e., MJD 54853.035) a frequency jump $\Delta\nu/\nu$ of $(1.9 \pm 1.6) \times 10^{-6}$, and frequency derivative jump $\Delta\dot{\nu}/\dot{\nu}$ of -0.69 ± 0.07. The frequency derivative jump value of $\Delta\dot{\nu} = +(1.30 \pm 0.14) \times 10^{-11}$ Hz s^{-1} indicates a dramatic sudden decrease of the spin-down rate, not seen before from any magnetar (Section 3.3.1; see also Section 7).
5. For the discontinuity in the timing behavior of 1E 1547.0−5408 near MJD 55121 (2009 October 17), we estimated from the incoherent timing models that a strong $\Delta\dot{\nu}/\dot{\nu}$ jump occurred of size (-0.89 ± 0.19), similar to the 2009 January 22 glitch. Note that this glitch was not accompanied by a radiative outburst (Section 3.3.2).

6.3. Pulsed Flux Evolution of 1E 1547.0−5408 below 10 keV

1. Applying our derived timing models for phase-folding barycentered *RXTE*/PCA event arrival times, we derived pulse-phase distributions for every PCA sub-observation. This allowed us to derive the pulsed-flux evolution for energies ∼2–10 keV from 2008 October 3 up to 2010 December 25 (see Section 3.4 and the bottom panel of Figure 1). Scholz & Kaspi (2011) showed a consistent evolution covering the first ∼150 days, including the two outburst epochs.
2. The evolution of the pulsed flux (energies ∼2–10 keV) behaves very different compared to that of the total flux below 10 keV: the radiative outburst of the pulsed flux in 2008 October is stronger than that in 2009 January, contrary to the findings for the total flux (Section 3.4 and Figure 1).
3. In 2008 October the pulsed flux (∼2–10 keV) reaches its maximum ∼10 days after the start of the outburst of the total emission (see the bottom panel of Figure 1). See also Ng et al. (2011) and Scholz & Kaspi (2011).
4. After the start of the 2009 January outburst the pulsed flux (∼2–10 keV) was unstable, varying by a factor of ∼2 for two weeks and then a linear decay set in over a period of almost 700 days with a decay rate of $(-6.15 \pm 0.66) \times 10^{-4}$ c (s day)$^{-1}$ (see Section 3.4 and the bottom panel of Figure 1).

6.4. Evolution of the Pulse-profile Morphology below ∼30 keV

1. Using *RXTE*/PCA monitoring data we constructed for 11 time segments between 2008 October 3 and 2010 December 25 pulse profiles in three X-ray bands: <4.14 keV (soft band), 4.14–11.22 keV (medium band), and 11.22–33.82 keV (hard band; Section 4 and Figure 8).
2. Between the onset of the 2008 October outburst and that of 2009 January, in the soft and medium bands a single broad pulse is detected with a peak at pulse phase ∼0.9. In the same time window the first evidence was found for weak pulsed emission in the hard band above 11 keV (Section 4 and Figure 8).
3. Drastic changes in pulse shape are found as a function of energy and of time after the glitch epoch and start of the radiative outburst in 2009 January: most notably, a transient hard X-ray pulse appears in the phase distribution after ∼11 days that can be well described with a Gaussian shape, centered at phase ∼0.59 and width (FWHM) 0.23. In the hard band above ∼11 keV this high-energy pulse is the single pulse detected; in the medium band this high-energy pulse is seen in addition to the broad pulse detected in the

soft band, which is similar but not identical to that detected in the soft and medium bands before the 2009 January outburst (Section 4.1, Figure 8; Section 4.2, Figure 9).
4. The new high-energy pulse reaches maximal flux in a time interval between 15 and 102 days after the onset of the 2009 January outburst and smoothly fades to undetectable levels within ∼350 days from the onset (Figure 9).
5. The time interval of ∼11 days after the glitch in 2009 January appears to be a transition period in which the pulse profile changes from the single broad soft pulse before the glitch to the structured pulse consisting of a soft and a transient hard component with peak phase separation ∼0.3. This ∼11 day time interval is also the period in which the pulsed flux (∼2–10 keV) was unstable, varying by a factor of ∼2 before a linear decay set in over a period of almost 700 days (see Figure 8 and for variability Section 3.4 and the bottom panel of Figure 1).

6.5. Evolution of the Pulsed Spectra for X-Ray Energies 2.5–150 keV

1. Exploiting the simultaneous monitoring with the PCA and HEXTE aboard *RXTE* we derived the spectra of the pulsed emission over the broad energy range 2.5–150 keV in 11 time segments between 2008 October 3 and 2010 December 25 (Section 5.1 and Figure 11).
2. Below ∼10 keV all pulsed-emission spectra are very soft with photon indices Γ in the range −[3.9–4.2], except in the first time segment (11 days; *RXTE* segment 3) after the 2009 January outburst (Γ ∼ −4.6). In the time period between the two outbursts, the flux (normalization) was highest during the first segment (26 days), decreased by a factor of ∼2 in the second segment (75 days) before the outburst in 2009 January. Promptly after the latter outburst, over a period of 11 days, the normalization was again higher by a factor of ∼2, followed by a gradual decrease by a factor of ∼2 over almost 700 days (Section 5.1 and Figure 11).
3. Around ∼10 keV the pulsed spectra change from very soft spectra to hard non-thermal spectra, with jumps in spectral photon index in the range 2.5–3.0 (Figure 11), similar to what has been reported for the persistent pulsed emission of some AXPs (e.g., Kuiper et al. 2006).
4. Above ∼10 keV the variations are more drastic than at lower energies. Between the 2008 October and 2009 January outbursts the pulsed emission above 10 keV was too weak to derive a spectrum. Directly after the 2009 January glitch/outburst, during the 11 days of segment 3, luminous pulsed hard X-ray emission was detected up to ∼150 keV. In the next time segment (no. 4) the maximal flux was reached at 70 ± 30 days after the glitch epoch, and a gradual decrease by more than a factor of 10 followed over a period of ∼300 days until the pulsed hard X-ray emission became undetectable. This spectral evolution follows the appearance and gradual fading of the hard X-ray pulse centered at phase ∼0.59 in the pulse profile (Sections 4.1 and 5.1; Figures 9 and 11).
5. During the periods with significant pulsed hard X-ray emissions, the total pulsed spectra over the broad energy range 2.5–150 keV can be satisfactorily described by a combination of a soft power-law (dominating below 10 keV) plus a cutoff power-law model (describing the hard X-ray emission). The latter component of the spectral fits reaches maxima in luminosity (in νF_ν) for energies in the range 90–105 keV and the power-law photon index varies with energy from ∼0 at 30 keV, ∼ − 1.2 at 70 keV to ∼ − 2 around 90 keV (Section 5.1).

The actual extrapolation of the spectral shape to higher energies (sharp break, bend?) is not constrained by our data.

6.6. Evolution of the Total Spectra for X-Ray Energies 1–300 keV

1. Making use of the imaging capabilities of *INTEGRAL*/ISGRI, JEM-X, and *Swift*/XRT, we derived the spectral evolution of the total emission of 1E 1547.0−5408 over the broad energy range 1–300 keV starting two days after the 2009 January glitch/outburst until 2010 April (Sections 5.2 and 5.3; Figure 13).
2. The total spectra can be satisfactorily described by a BB plus a single Pl model over the full 1–300 keV band. The BB component was found to have kT values varying in the range 0.57–0.74 keV. The photon index of the power-law component exhibited a hardening with time and a clear correlation with flux in the 20–150 keV band, namely, its value gradually changed from ∼−1.4 directly after the glitch in 2009 January to ∼−0.9 in 2010 February–April, while the 20–150 keV flux decreased by a factor of ∼3 (Section 5.4, Table 8, and Figure 13).
3. The total soft X-ray flux (1–10 keV) measured with *Swift*/XRT (contributions from the BB plus Pl components) is maximal during the first *INTEGRAL* observation two days after the glitch and decays similarly to what we measured for the count rates below 10 keV with *RXTE*/PCA (Section 5.4; Figures 13 and 14).
4. The total hard X-ray flux (20–150 keV) measured with *INTEGRAL*/ISGRI is also directly maximal in the first observation two days after the glitch in 2009 January, decaying in flux by a factor of ∼3 until 2010 February–April, when the source was still detected in the sky map at a 9.5σ level in the 20–150 keV band (Section 5.3; Figures 12, 13, and 14). This behavior is in contrast to what we measured for the evolution of the pulsed hard X-ray component: the latter reached maximal flux 70 ± 30 days after the glitch, subsequently decaying to undetectable levels in ∼300 days, a decrease in flux by more than a factor of 10 (Figures 9 and 11).

7. DISCUSSION

The above summarized results on the evolution of the high-energy characteristics of 1E 1547.0−5408 over a period of 27 months, addressing the timing parameters, pulse morphologies, total and pulsed spectra in the soft and hard X-ray bands, provide important constraints on the theoretical modeling of the production scenarios in the magnetosphere. Particularly interesting is that for the first time from the start of an outburst, accompanied by a timing glitch, not only the evolution at soft X-ray energies could be studied in detail, but also at (non-thermal) hard X-ray energies, and the behaviors of distinctly different components compared. The measured timing glitch in 2009 January is itself already interesting, so far being the most extreme *instantaneous* frequency derivative jump $\Delta\dot{\nu}/\dot{\nu}$ of -0.69 ± 0.07 detected, with $\Delta\dot{\nu} = +(1.30 \pm 0.14) \times 10^{-11}$ Hz s^{-1}.

We scrutinized earlier publications on magnetar (SGR/AXP) timing, mainly based on *RXTE* observations, and focused on frequency derivative jumps $\Delta\dot{\nu}/\dot{\nu}$ with *negative* signs of order unity. Although large gradual $\dot{\nu}$ fluctuations are reported for

SGR 1900+14 (Woods et al. 1999, 2002) and SGR 1806−20 (Woods et al. 2002, 2007), no convincing *sudden* instantaneous $\dot{\nu}$ jumps are detected. A possibly similar event as observed for 1E 1547.0−5408 may have occurred for SGR 1900+14 (Woods et al. 2002) near its 1998 August 27 giant flare of size $\Delta\dot{\nu}/\dot{\nu} \sim -0.28$, but due to a ∼80 days data gap in the *RXTE* timing observations prior to the giant flare a gradual accelerated spin-down could not be excluded. A radiative (pulsed and persistent emission) outburst, accompanied with a timing glitch, has been reported by Kaspi et al. (2003) for AXP 1E 2259+586, but the measured $\Delta\dot{\nu}/\dot{\nu}$ jump of +1.11 has positive sign, and the absolute value of the $\Delta\dot{\nu}$ jump is orders of magnitude smaller than that observed for 1E 1547.0−5408. Also, the glitches with a measurable $\Delta\dot{\nu}$ jump detected from AXPs 1RXS J1708−40 (Dib et al. 2008), 1E 1841−045 (Dib et al. 2008), 4U 0142+614 (Dib et al. 2007; Gavriil et al. 2011), and 1E 1048.1−5937 (Dib et al. 2009) do not show the magnitude, sign, and relative strength as observed for 1E 1547.0−5408, making the latter glitch unique.

The dramatic decrease in spin-down rate, observed for 1E 1547.0−5408 during the 2009 January 22 glitch, would for purely dipole spin-down naively imply a decrease in effective surface dipole field strength by ∼50%. In the twisted magnetosphere model such a drastic change in $\dot{\nu}$ and B might be due to a varying twist angle with corresponding spectral and flux changes (Beloborodov & Thompson 2007). The epoch of the timing glitch is consistent with the start of the outburst, therefore, we assume that the glitch triggered the outburst on MJD 54853.035 (TDB), 2009 January 22. It is then intriguing that there are no signs of a radiative outburst near MJD 55121, 2009 October 17, for which our analysis suggests a similarly strong $\Delta\dot{\nu}/\dot{\nu}$ jump.

Recently published works on 1E 1547.0−5408 the analyses of which were performed in parallel to our work, focused primarily on the evolution of the (pulsed) emission below 10 keV in time intervals up to ∼20 days after the outbursts in 2008 October and 2009 January (Ng et al. 2011; Bernardini et al. 2011; Scholz & Kaspi 2011), as we summarized in the Introduction.

In our work, we revealed in addition the creation of a new transient non-thermal pulse in the pulse phase distribution after the 2009 January glitch, and could study the simultaneous evolution of the pulsed and total high-energy emissions, the latter being dominated by an unpulsed component (∼65%). It is striking that the spectrum of the pulsed emission from 2 keV up to 150 keV after the glitch is very similar to the shapes of the broadband spectra of the persistent pulsed emissions of three AXPs, 1E 1841−045, 4U 0142+61, and 1RXS J1708−40 (Kuiper et al. 2006; den Hartog et al. 2008a, 2008b). The non-thermal pulsed component (20–150 keV) of 1E 1547.0−5408 reaches in the time interval 15–101 days after the glitch (*RXTE* time segment 4; see Table 5) a flux of $(7.5^{+0.9}_{-1.0}) \times 10^{-11}$ erg cm^{-2} s^{-1} (see Table 6) and an (isotropic) luminosity of $\sim 13.6 \times 10^{34}$ erg s^{-1} adopting the distance estimate of 3.9 kpc of Tiengo et al. (2010), which is about 1.4 times the spin-down luminosity during that time segment. There are clearly two maxima in the luminosity distribution of the pulsed spectrum, one around 100 keV and one near 1 keV (the maximum, likely due to a BB component, is reached below our energy interval; earlier works did not address the spectra of the *pulsed* emission of 1E 1547.0−5408 below 10 keV, nor above 10 keV). We also see a clear phase separation of ∼0.3 between the soft-spectrum pulse and the hard non-thermal pulse, similar to the case of 1RXS J1708−40 (e.g., den Hartog et al. 2008a). In fact, the broadband total spectrum is also reminiscent of those measured for these three persistent AXPs. However, for 1E 1547.0−5408 we are dealing with a transient/variable phenomenon above (and below) 10 keV, while it was found that the non-thermal persistent emission of AXPs appeared stable within the statistical errors of ∼20% over more than 10 years.

The steadiness of the persistent non-thermal emission from AXPs led Beloborodov (2009, 2011) to reconsider his scenarios proposed earlier to explain the production of this non-thermal component (Beloborodov & Thompson 2007). As mentioned in the Introduction, he discusses how a starquake can cause convective motions in the crust which twist the external magnetic field anchored to the surface. The magnetic twist energy is dissipated over time in the form of radiation, but the untwisting occurs in a peculiar way leading to the creation of a bundle of electric currents, the so-called j-bundle, which shrinks toward the magnetic dipole axis. The high-energy component, created by upscattering of thermal X-rays from the neutron star surface by an inner relativistic outflow in the quasi-steady j-bundle, is beamed along the magnetic dipole axis. The latter can explain the relatively narrow high-energy pulses. Furthermore, his radiative-transfer simulations produce spectral shapes that get close to those observed, but with possibly too high of break energies near 1 MeV.

It is very interesting to note that a radiative outburst accompanied by a strong glitch in the case of 1E 1547.0−5408 indeed led to a scenario/geometry which mimics in many respects the observational characteristics of the persistent emission seen from AXPs. But our results on 1E 1547.0−5408 pose several new observational constraints on this model scenario, as well as on other theoretical attempts (none of the other models addresses the transient hard X-ray (>20 keV) phenomenon of the persistent emission). A constraint on the timescale of creation of the quasi-steady narrow j-bundle is the delay with respect to the glitch epoch of 70±30 days, with which the high-energy pulse with non-thermal spectrum was created. Another important finding is that the total non-thermal high-energy emission was present immediately in the first *INTEGRAL* observation starting two days after the glitch. This suggests that there should be a "corona" around the neutron star in which non-thermal unpulsed emission is produced without delay already at the start of the outburst. The model scenario of Beloborodov (2009, 2011) was proposed to explain the steady non-thermal emission from AXPs. What we find is a transient pulsed component which decays by a factor of $\gtrsim$10, becoming undetectable ∼300 days after the glitch. However, the non-thermal total (pulsed+unpulsed) emission decayed only by a factor of ∼3 over more than a year, seemingly stable over the last ∼100 days. A possibility is that a steady state similar to that of persistent emission of the above-mentioned AXPs was reached after about one year, but that the pulsed non-thermal emission has become too weak to be detectable with currently operational high-energy instruments. The situation might be representative for all those AXPs for which no non-thermal emission has been detected (yet), but all have X-ray fluxes in the transition region around 10 keV that also are weaker than detected for the AXPs with reported steady non-thermal persistent emission above 20 keV up to ∼150 keV. In this respect, we like to note that 1E 1547.0−5408 was in the field of view of *INTEGRAL* during Revs. 470–572 (2006 August 21–2007 June 22) for an effective exposure of 227.2 ks during a period in which the soft X-ray flux state increased at least 16 times its historical flux minimum reached in 2006 July–August. Halpern et al. (2008) concluded that the source was then

recovering from an X-ray outburst between 2006 August and 2007 June. However, we did not find evidence for an outburst of non-thermal emission above 20 keV from 1E 1547.0−5408 in the *INTEGRAL*/ISGRI sky maps. The 2σ upper limits to the flux measurements are at the level of the positive flux measurements in Revs. 899–912 (around 2010 March) in Figure 13, but still significantly higher than the low flux upper limits from the very deep summed exposure before 2006 (Revs. 46–411 in Figure 13). Also in this case we cannot exclude the scenario proposed by Beloborodov (2009, 2011) because the total and particularly pulsed emission from AXPs and also from SGRs is (too) weak for easy detection by presently operational instruments.

We noted the importance of studying the characteristics of magnetars over a broad energy interval. In the case of 1E 1547.0−5408 we concluded that discussions based on spectral model fits to the narrow energy range 1–10 keV (e.g., Scholz & Kaspi 2011) lead to apparent characteristics (e.g., power-law component with spectral softening with decreasing flux) which have to be revised when the broad energy range is considered, including the hard X-rays (power-law component with spectral hardening with decreasing flux). Furthermore, broadband studies of the magnetar class are now becoming possible, as has been published by Enoto et al. (2010b) using *Suzaku* observations of a sample of eight magnetars, including 1E 1547.0−5408 in outburst. In that paper interesting correlations have been studied for the total emission of the hardness ratio, defined as the ratio of the flux of the hard, non-thermal component (Pl fit; 1–60 keV) and the flux of the soft component (a BB, a Comptonized BB, or a combination of the two; 1–60 keV) with derived characteristics as, e.g., characteristic age and magnetic field strength. Such a study ignores, however, that the origins of the actual unpulsed and pulsed emissions appear to be different (location in the magnetosphere, production scenario) as is evidenced by the different spectra of the pulsed and total (pulsed+unpulsed) emissions (particularly above 10 keV), the different pulse profiles (shape and phase) for soft and hard pulsed components, and the different evolutions of all contributing components. Theoretical modeling of the physics taking place under the extreme conditions in magnetospheres of magnetars is extremely complex. It is encouraging that the amount and detail of observational constraints is increasing significantly over the last few years.

We acknowledge the use of public data from the *Swift* data archive. This research has made use of data obtained from the High Energy Astrophysics Science Archive Research Center (HEASARC), provided by NASA's Goddard Space Flight Center, and of data obtained through the *INTEGRAL* Science Data Centre (ISDC), Versoix, Switzerland. *INTEGRAL* is an ESA project with instruments and science data center funded by ESA member states (especially the PI countries: Denmark, France, Germany, Italy, Switzerland, Spain), Czech Republic, and Poland, and with the participation of Russia and the United States. We have extensively used NASA's Astrophysics Data System (ADS). This work has been supported by NASA grant NNX10AJ54G.

REFERENCES

Alpar, M. A. 2001, ApJ, 554, 1245
Baldovin, C., Savchenko, V., Beckman, V., et al. 2009, ATel, 1908
Baring, M. G., & Harding, A. K. 2007, Ap&SS, 308, 109
Baring, M. G., & Harding, A. K. 2008, in AIP Conf. Proc. 968, Astrophysics of Compact Objects, ed. Y.-F. Yuan, X.-D. Li, & D. Lai (Berlin: Springer), 93
Bellm, E., Smith, D. M., & Hurley, K. 2009, GCN Circ., 8857, 1
Beloborodov, A. M. 2009, ApJ, 703, 1044
Beloborodov, A. M. 2011, in Astrophys. Space Sci. Proc., High-energy Emission from Pulsars and Their Systems, ed. N. Rea & D. F. Torres (Berlin: Springer), 299
Beloborodov, A. M., & Thompson, C. 2007, ApJ, 657, 967
Bernardini, F., Israel, G. L., Stella, L., et al. 2011, A&A, 529, A19
Buccheri, R., Bennett, K., Bignami, G., et al. 1983, A&A, 128, 245
Burrows, D. N., Hill, J. E., Nousek, J. A., et al. 2005, Space Sci. Rev., 120, 165
Camilo, F., Ransom, S. M., Halpern, J. P., et al. 2006, Nature, 442, 892
Camilo, F., Ransom, S. M., Halpern, J. P., et al. 2007, ApJ, 666, L93
Camilo, F., Reynolds, J., Johnston, S., et al. 2008, ApJ, 679, 681
Chatterjee, P., Hernquist, L., & Narayan, R. 2000, ApJ, 534, 373
Connaughton, V., & Briggs, M. 2009, GCN Circ., 8835, 1
Courvoisier, T. J.-L., Walter, R., Beckmann, V., et al. 2003, A&A, 411, L53
den Hartog, P. R., Kuiper, L., & Hermsen, W. 2008a, A&A, 489, 263
den Hartog, P. R., Kuiper, L., & Hermsen, W. 2009, ATel, 1922
den Hartog, P. R., Kuiper, L., Hermsen, W., et al. 2008b, A&A, 489, 245
Dib, R., Kaspi, V. M., & Gavriil, F. P. 2007, ApJ, 666, 1152
Dib, R., Kaspi, V. M., & Gavriil, F. P. 2008, ApJ, 673, 1044
Dib, R., Kaspi, V. M., & Gavriil, F. P. 2009, ApJ, 702, 614
Duncan, R. C., & Thompson, C. 1992, ApJ, 392, L9
Enoto, T., Nakazawa, K., Makishima, K., et al. 2010a, PASJ, 62, 475
Enoto, T., Nakazawa, K., Makishima, K., et al. 2010b, ApJ, 722, L162
Esposito, P., Israel, G. L., Turolla, R., et al. 2011, MNRAS, 416, 205
Falanga, M., Kuiper, L., Poutanen, J., et al. 2005, A&A, 444, 15
Falanga, M., Kuiper, L., Poutanen, J., et al. 2011, A&A, 529, 68
Fernandez, R., & Thompson, C. 2007, ApJ, 660, L615
Gavriil, F. P., Dib, R., & Kaspi, V. M. 2011, ApJ, 736, 138
Gehrels, N., Chincarini, G., Giommi, P., et al. 2004, ApJ, 611, 1005
Gelfand, J. D., & Gaensler, B. M. 2007, ApJ, 667, 1111
Göğüş, E., Cusumano, G., Levan, A. J., et al. 2010a, ApJ, 718, 331
Göğüş, E., Güver, T., Özel, F., et al. 2011, ApJ, 728, 160
Göğüş, E., Woods, P. M., Kouveliotou, C., et al. 2010b, ApJ, 722, 899
Golenetskii, S., Aptekar, R., Mazets, E., et al. 2009, GCN Circ., 8851, 1
Götz, D., Mereghetti, S., Tiengo, A., & Esposito, P. 2006, A&A, 449, L31
Gronwall, C., Holland, S. T., Markwardt, C. B., et al. 2009, GCN Circ., 8833, 1
Güver, T., Özel, F., Göğüş, E., & Kouveliotou, C. 2007, ApJ, 667, L73
Güver, T., Özel, F., & Göğüş, E. 2008, ApJ, 675, 1499
Halpern, J. P., Gotthelf, E. V., Reynolds, J., et al. 2008, ApJ, 676, 1178
Israel, G. L., Esposito, P., Rea, N., et al. 2010, MNRAS, 408, 1387
Jahoda, K., Swank, J. H., Giles, A. B., et al. 1996, Proc. SPIE, 2808, 59
Jourdain, E., & Roques, J. P. 2008, Proc. Sci. (Integral08), 143 (http://pos.sissa.it/cgi-bin/reader/conf.cgi?confid=67)
Kaneko, Y., Göğüş, E., Kouveliotou, C., et al. 2010, ApJ, 710, 1335
Kaspi, V. M. 2007, Ap&SS, 308, 1
Kaspi, V. M., Gavriil, F. P., Woods, P. M., et al. 2003, ApJ, 588, L93
Krimm, H. A., Beardmore, A. P., Burrows, D. N., et al. 2008a, GCN Circ., 8311, 1
Krimm, H. A., Beardmore, A. P., Gehrels, N., et al. 2008b, GCN Circ., 8312, 1
Kuiper, L., den Hartog, P. R., & Hermsen, W. 2009, ATel, 1921
Kuiper, L., & Hermsen, W. 2009, A&A, 501, 1031
Kuiper, L., Hermsen, W., den Hartog, P. R., & Collmar, W. 2006, ApJ, 645, 556
Kuiper, L., Hermsen, W., & Mendeź, M. 2004, ApJ, 613, 1173
Kuiper, L., Jonker, P. G., Torres, M. A. P., et al. 2008, ATel, 1774
Lamb, R. C., & Markert, T. H. 1981, A&A, 244, 94
Lebrun, F., Leray, J. P., Lavocat, P., et al. 2003, A&A, 411, L141
Lund, N., Budtz-Jørgensen, C., Westergaard, N. J., et al. 2003, A&A, 411, L231
Lyutikov, M., & Gavriil, F. P. 2006, MNRAS, 368, 690
Malheiro, M., Rueda, J., & Ruffini, R. 2011, A&A, submitted (arXiv:1102.0653)
Mereghetti, S. 2008, A&AR, 15, 225
Mereghetti, S., Götz, D., von Kienlin, A., et al. 2009a, GCN Circ., 8841, 1
Mereghetti, S., Götz, D., Weidenspointer, G., et al. 2009b, ApJ, 696, L74
Ng, C.-Y., Kaspi, V. M., Dib, R., et al. 2011, ApJ, 729, 131
Nobili, L., Turolla, R., & Zane, S. 2008, MNRAS, 386, 1527
Orsaria, M., Ranea-Sandoval, I., & Vucetich, H. 2011, ApJ, 734, 41
Pavan, L., Turolla, R., Zane, S., & Nobili, L. 2009, MNRAS, 395, 753
Rea, N., Israel, G. L., Turolla, R., et al. 2009, MNRAS, 396, 2419
Rea, N., Zane, S., Turolla, R., et al. 2008, ApJ, 686, 1245
Rothschild, R. E., Blanco, P. R., Gruber, D. E., et al. 1998, ApJ, 496, 538
Savchenko, V., Beckmann, V., Neronov, A., et al. 2009, GCN Circ., 8837, 1
Savchenko, V., Neronov, A., Beckmann, V., et al. 2010, A&A, 510, A77
Scholz, P., & Kaspi, V. M. 2011, ApJ, 739, 94
Terada, Y., Tashiro, M., Urata, Y., et al. 2009, GCN Circ., 8845, 1
Thompson, C., & Duncan, R. C. 1995, MNRAS, 275, 255
Thompson, C., Lyutikov, M., & Kulkarni, S. R. 2002, ApJ, 574, 332
Tiengo, A., Vianello, G., Esposito, P., et al. 2010, ApJ, 710, 227

Trümper, J. E., Kylafis, N. D., Ertan, Ü., & Zezas, A. 2010a, A&A, submitted (arXiv:1011.1678)
Trümper, J. E., Zezas, A., Ertan, Ü., & Kylafis, N. D. 2010b, A&A, 518, 46
Ubertini, P., Lebrun, F., Di Cocco, G., et al. 2003, A&A, 411, L131
Vedrenne, G., Roques, J.-P., Schönfelder, V., et al. 2003, A&A, 411, L63
Vink, J., & Bamba, A. 2009, ApJ, 707, L148
von Kienlin, A., & Briggs, M. S. 2008, GCN Circ., 8315, 1
Winkler, C., Courvoisier, T. J.-L., Di Cocco, G., et al. 2003, A&A, 411, L1
Woods, P. M., Kaspi, V. M., Gavriil, F. P., & Airhart, C. 2011, ApJ, 726, 37
Woods, P. M., Kaspi, V. M., Thompson, C., et al. 2004, ApJ, 605, 378
Woods, P. M., Kouveliotou, C., Finger, M. H., et al. 2007, ApJ, 654, 470
Woods, P. M., Kouveliotou, C., Göğüş, E., et al. 2002, ApJ, 576, 381
Woods, P. M., Kouveliotou, C., van Paradijs, J., et al. 1999, ApJ, 524, L55
Woods, P. M., & Thompson, C. 2006, in Compact Stellar X-Ray Sources, ed. W. Lewin & M. van der Klis (Cambridge: Cambridge Univ. Press), 547
Xu, R. 2007, Adv. Space Res., 40, 1453
Zane, S., Rea, N., Turolla, R., et al. 2009, MNRAS, 398, 1403
Zane, S., Turolla, R., Nobili, L., & Rea, N. 2011, Adv. Space Res., 47, 1298